



# A machine-learning digital-twin for rapid large-scale solar-thermal energy system design

T.I. Zohdi

*Department of Mechanical Engineering, University of California, Berkeley, CA, 94720-1740, USA*

Received 18 February 2023; accepted 4 March 2023

Available online 25 May 2023

## Abstract

In many industrialized regions of the world, large-scale photovoltaic systems now contribute a significant part to the energy portfolio during daylight operation. However, as energy demands peak shortly before sunset and persist for several hours afterwards, the integration of solar-thermal systems is extremely advantageous as a green “bridge” energy source. Accordingly, this work develops a digital-twin model to track and optimize the flow of incoming solar power through a complex solar-thermal storage system, consisting of a large array of adaptable mirrors, an optical-receiver and a power distribution system for customers to extract energy. Specifically, the solar power flow is rapidly computed with a reduced order model of Maxwell’s equations, based on a high-frequency decomposition of the irradiance into multiple rays that experience mirror reflections, losses and ultimately receiver absorption and customer delivery. The method allows for rapid testing (in microseconds) of the performance of large numbers of mirror-receiver layout configurations in design space, over extremely long time periods, such as weeks, months and years, using a genetic-based machine-learning digital-twin framework, which integrates submodels for:

- optics and tracking of the Fresnel multi-mirror system,
- thermal absorption of the optical energy by the receiver and
- optimal operating temperatures balancing radiative losses with heat storage.

The overall machine-learning digital-twin optimizes the configuration layout to balance meeting customer demands and operational efficiency. Numerical examples are provided to illustrate the approach. Finally, a deep-learning algorithm is developed and applied to the create an Artificial Neural-Net representation, which allows for even further simulation speedup. © 2023 Published by Elsevier B.V.

*Keywords:* Solar-thermal; Energy management systems; Digital-twin; Machine-learning

## 1. Introduction

In many industrialized regions of the world, large-scale photovoltaic systems now contribute a significant part to the energy portfolio during daylight operation. However, as energy demands peak shortly before sunset and persist for several hours afterwards, the integration of solar-thermal systems (using Concentrated Solar Power (CSP) for energy storage) is extremely advantageous as a green “bridge” energy source. Solar-thermal systems often employ (1) molten salt storage and (2) a steam turbine and generator for electricity. The central tower approach (Fig. 1) is considered the most efficient type of configuration (as opposed to arrays of local concentrators).

*E-mail address:* [zohdi@berkeley.edu](mailto:zohdi@berkeley.edu).

<https://doi.org/10.1016/j.cma.2023.115991>

0045-7825/© 2023 Published by Elsevier B.V.

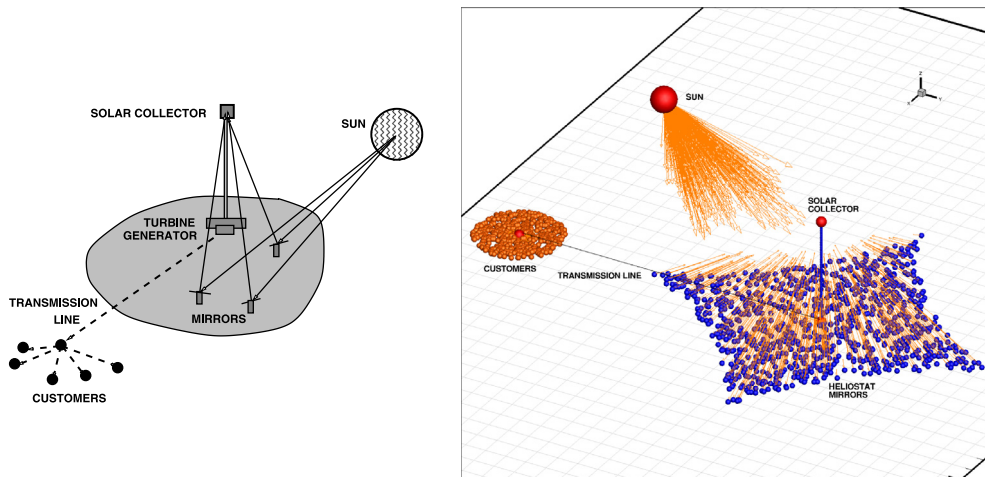


**Fig. 1.** Left, overall solar-thermal system and right, a snapshot of an upcoming simulation comprised of (a) the movement of a source (sun), (b) a configuration of adaptive mirrors, (c) a solar collector with a turbine and generator and (d) customers connected by a transmission line.

The present work develops a digital-twin model to track and optimize the flow of incoming solar power through a complex solar-thermal storage system, consisting of a large array of adaptable mirrors, an optical-receiver and a power distribution system for customers to extract energy. Specifically, the solar power flow is rapidly computed with a reduced order model of Maxwell's equations, based on a high-frequency decomposition of the irradiance into multiple rays that experience mirror reflections, losses and ultimately receiver absorption and customer delivery. The method allows for rapid testing (in microseconds) of the performance of large numbers of mirror-receiver layout configurations in design space, over extremely long time periods, such as weeks, months and years, using a genetic-based machine-learning digital-twin framework, which integrates submodels for:

- optics and tracking of the Fresnel multi-mirror system,
- thermal absorption of the optical energy by the receiver and
- optimal operating temperatures balancing radiative losses with heat storage.

The overall machine-learning digital-twin optimizes the configuration layout to balance meeting customer demands and operational efficiency. Numerical examples are provided to illustrate the approach. Finally, a deep-learning algorithm is developed and applied to the create an Artificial Neural-Net representation, which allows for even further simulation speedup. This system modeling falls into the category of a Green Energy Management System (EMS) planner. EMS refer to frameworks that control the energy generation, transmission and storage for multiple devices which are coupled. These can range from systems for nationwide grids, utility-scale systems, microgrids, data-centers and electric vehicles (Fig. 1) and can consist of renewable energy sources, fossil-fuel energy, transmission lines, batteries, generators, ultracapacitors and transformers. The goals of such systems are typically to balance the load, guarantee the power supply for each device, maximize overall efficiency and to minimize overall losses. In Zohdi [1], a detailed “macroscale” analysis of EMS and optimization was undertaken, which balanced storage, transmission and consumption of multiple interconnected units, using machine-learning paradigms. One motivation for the development of next generation Green Energy Management Systems is the exponential increase in data-centers, which we define as locations dedicated to housing computer systems comprised of data handling units, telecommunications, high-performance computing devices and associated equipment. Between 2010 and 2018, the global quantity of data traversing the internet increased more than ten-fold, while global data-center storage capacity increased by a factor of twenty-five in that same period (Masanet et al. [2]). While the analysis of the energy trends are hotly debated, one point of agreement is that energy demands are consistently increasing, year after year, in part because of the huge increase in internet traffic and staggering increase data-centers. The reader is referred to [3–26] for a wide swath of the literature on this topic. All data indicate that the costs of such systems is huge and growing rapidly. The basic trends on energy consumption by data-centers can be found in the extensive report of Shehabi et al. [27].

**Remark 1.** In order to grasp the immensity of available solar power, consider a rough estimate assuming: (a) the Earth’s radius:  $R \approx 6,400,000$  m, (b) the Earth’s surface area:  $A \approx 4\pi R^2$ , (c) the peak solar power per unit area:  $p \approx 1300$  Watts/m<sup>2</sup>, (d) the assumption that roughly 1/2 of the Earth is illuminated at any given time and (e) the overall surface achieves 1/2 peak illumination (on average) yields an estimate of  $P = \frac{Ap}{4} \approx 167,358$  terawatts. The actual number is approximately 173,000 terawatts (NREL [28]), which is approximately 10,000 times the worldwide power usage in 2019–2020.

**Remark 2.** In Zohdi [29], an in-depth “microscale” analysis was conducted to optimize a data-center’s power management by controlling both the ventilation and base foundation cooling of the data processors in the system. That framework ascertained optimal cooling strategies to deliver a target system temperature using a minimum amount of energy. A thermo-fluid model, based on the Navier–Stokes equations and the first law of thermodynamics, for the data-center was constructed and a rapid, voxel-based, iterative solution method was developed and combined with a genetic-based machine-learning algorithm to develop a digital-twin of the system that could run in real-time or faster than the actual physical system, making it suitable as either a design tool or an adaptive controller. In the present analysis, we develop a macroscale solar-thermal system for efficient green energy delivery for such subsystems, among others.

## 2. Model problem: a coupled multi-device system

There are four main components in the system to be modeled:

- the configuration of mirrors, which focus solar power onto the storage system (receiver),
- the solar thermal storage (receiver) system, which delivers energy to customers (power consuming devices),
- the transmission network, which incurs electromechanical losses, as well as joule-heating losses and
- the customers, which can consume and possibly generate energy.

Algorithmically, the overall system operates in the following manner:

1. Optical energy that flows from the sun to the tracking mirrors,
2. Mirrors are controlled to orient themselves to reflect light towards the optical receiver (there are reflective losses and tracking motor losses),
3. The optical receiver system absorbs energy and stores it (there are thermal radiation losses),
4. A turbine-generator system produces electricity for customers on demand (incurring thermo-mechanical and transmission losses) and
5. Customers induce a load onto the system that contribute to overall system losses.

## 3. Digital-twin structure and reduced-order model for optical energy flow

### 3.1. Assumptions for reduced-order model

The interest here is on the reflection of rays towards a target receiver. We make the following observations (following Zohdi [30–36]):

- It is assumed that the features of the surfaces that receive optical power are at least an order of magnitude larger than the wavelength of the incident radiation (essentially specular (non-diffusive) optical surfaces), therefore “geometrical” ray-tracing theory is applicable, and is well-suited for the systems of interest. It is important to emphasize the regimes of validity of such a model are cases where the surface features are larger than the optical wavelengths. For example, if we were to use rays ( $10^{-8} \text{ m} \leq \lambda \leq 4 \times 10^{-7} \text{ m}$ ), the features in this analysis would be assumed to possess scales larger than approximately  $4 \times 10^{-6} \text{ m}$ . For systems containing features smaller than this, one can simply use the model as a qualitative guide.
- Ray-tracing is a method that is employed to produce rapid approximate solutions to wave-equations for high-frequency/small-wavelength applications where the primary interest is in the overall propagation of power.<sup>1</sup>

<sup>1</sup> Resolving diffraction (which ray theory is incapable of describing) is unimportant for the applications of interest.

- Ray-tracing methods proceed by initially representing wave fronts by an array of discrete rays. *Thereafter, the problem becomes one of a primarily geometric character*, where one tracks the changing trajectories and magnitudes of individual rays which are dictated by the reflectivity and the Fresnel conditions (if a ray encounters a material interface).
- Ray-tracing methods are well-suited for computation of scattering in complex systems that are difficult to mesh/discretize, relative to procedures such as the Finite Difference Time Domain Method or the Finite Element Method.
- Other high frequency irradiation regimes can also be considered in the same manner, such as UV, X-rays and gamma rays, provided that the scattering target has the appropriate (larger) length-scale. Even in the case where this clear separation of length scales is not present, this model still provides valuable information on the propagation of the beam and the reflected response of the dispersed system.

Note the connection of the concept of a ray:

- We define  $\bar{I}$  as the power per unit area, and we obtain the power by multiplying the irradiance by the area of the mirror  $\bar{I}A^m$ .
- The power for each ray is then collected at the optical receiver, after being reflected.
- Fresnel reflection relations can then be used to compute changes in the magnitude of the reflected rays (and the amount absorbed), with directional changes given by the laws of reflection.

Essentially, rays are a mathematical construction/discretization of a pulse/beam. We refer the reader to Gross [37], Zohdi [30–36] for details. From this point forth, we assume that the ambient medium behaves as a vacuum. Accordingly, there are no appreciable energetic losses as the rays move through the atmosphere.

### 3.2. Reflection and absorption of rays

Following a framework found in Zohdi [30–36], we consider a ray of light incident upon a material interface, which produces a reflected ray and a transmitted/absorbed (refracted) ray (Fig. 2), the amount of incident electromagnetic (optical) power ( $I_i$ ) that is reflected ( $I_r$ ) is given by the total reflectance  $\mathcal{R} \stackrel{\text{def}}{=} \frac{I_r}{I_i}$ , where  $0 \leq \mathcal{R} \leq 1$ .

### 3.3. Electromagnetic wave propagation and rays

The propagation of electromagnetic waves in free space can be described by a simplified form of Maxwell's equations (see Jackson [38], Zohdi [33])

$$\nabla \times \mathbf{E} = -\mu_o \frac{\partial \mathbf{H}}{\partial t}, \quad \text{and} \quad \nabla \times \mathbf{H} = \epsilon_o \frac{\partial \mathbf{E}}{\partial t}, \quad (3.1)$$

where  $\nabla \cdot \mathbf{H} = 0$ ,  $\nabla \cdot \mathbf{E} = 0$ ,  $\mathbf{E}$  is the electric field,  $\mathbf{H}$  is the magnetic field,  $\epsilon_o$  is the free space permittivity and  $\mu_o$  is the free space permeability. Using standard vector identities, one can show that

$$\nabla \times (\nabla \times \mathbf{E}) = -\mu_o \epsilon_o \frac{\partial^2 \mathbf{E}}{\partial t^2}, \quad \text{and} \quad \nabla \times (\nabla \times \mathbf{H}) = -\mu_o \epsilon_o \frac{\partial^2 \mathbf{H}}{\partial t^2}, \quad (3.2)$$

and that

$$\nabla^2 \mathbf{E} = \frac{1}{c^2} \frac{\partial^2 \mathbf{E}}{\partial t^2}, \quad \text{and} \quad \nabla^2 \mathbf{H} = \frac{1}{c^2} \frac{\partial^2 \mathbf{H}}{\partial t^2}, \quad (3.3)$$

where the speed of electromagnetic waves is  $c = \frac{1}{\sqrt{\epsilon_o \mu_o}}$ . All electromagnetic radiation travels, in a vacuum, at the speed  $c \approx 2.99792458 \times 10^8 \pm 1.1$  m/s. In any another medium, for electromagnetic waves, the propagation speed is  $v = \frac{1}{\sqrt{\epsilon \mu}}$ , where  $\epsilon$  and  $\mu$  are the electric permittivity and magnetic permeability of that medium, respectively.<sup>2</sup>

<sup>2</sup> The free space electric permittivity is  $\epsilon_o = \frac{1}{c^2 \mu_o} = 8.8542 \times 10^{-12}$  CN<sup>-1</sup>m<sup>-1</sup> and the free space magnetic permeability is  $\mu_o = 4\pi \times 10^{-7}$  WbA<sup>-1</sup>m<sup>-1</sup> = 1.2566 × 10<sup>-6</sup> WbA<sup>-1</sup>m<sup>-1</sup>.

### 3.4. Plane harmonic wave fronts

Now consider the special case of plane harmonic waves, for example of the form

$$\mathbf{E} = \mathbf{E}_o \cos(\mathbf{k} \cdot \mathbf{x} - \omega t) \quad \text{and} \quad \mathbf{H} = \mathbf{H}_o \cos(\mathbf{k} \cdot \mathbf{x} - \omega t), \tag{3.4}$$

where  $\mathbf{x}$  is an initial position vector to the wave front, where  $\mathbf{k}$  is the direction of propagation. We refer to the phase as  $\phi = \mathbf{k} \cdot \mathbf{x} - \omega t$ , and  $\omega = \frac{2\pi}{\tau}$  as the angular frequency, where  $\tau$  is the period. For plane waves, the wave front is a plane on which  $\phi$  is constant, which is orthogonal to the direction of propagation, characterized by  $\mathbf{k}$ . In the case of harmonic waves, we have

$$\mathbf{k} \times \mathbf{E} = \mu_o \omega \mathbf{H} \quad \text{and} \quad \mathbf{k} \times \mathbf{H} = -\epsilon_o \omega \mathbf{E}, \tag{3.5}$$

and  $\mathbf{k} \cdot \mathbf{E} = 0$  and  $\mathbf{k} \cdot \mathbf{H} = 0$ . The three vectors,  $\mathbf{k}$ ,  $\mathbf{E}$  and  $\mathbf{H}$  constitute a mutually orthogonal triad.<sup>3</sup> The direction of wave propagation is given by  $\frac{\mathbf{E} \times \mathbf{H}}{\|\mathbf{E} \times \mathbf{H}\|}$ . Electromagnetic waves traveling through space carry electromagnetic power which flows in the direction of wave propagation. The power per unit area flowing perpendicularly into a surface in free space is given by the Poynting vector  $\mathbf{S} = \mathbf{E} \times \mathbf{H}$ .

### 3.5. Natural (random) electromagnetic power propagation

Since at high-frequencies  $\mathbf{E}$ ,  $\mathbf{H}$  and  $\mathbf{S}$  oscillate rapidly, it is impractical to measure instantaneous values of  $\mathbf{S}$  directly. Consider the harmonic representations in Eq. (3.4) which leads to  $\mathbf{S} = \mathbf{E}_o \times \mathbf{H}_o \cos^2(\mathbf{k} \cdot \mathbf{x} - \omega t)$ , and consequently the average value over a longer time interval ( $\mathcal{T}$ ) than the time scale of rapid random oscillation,

$$\langle \mathbf{S} \rangle_{\mathcal{T}} = \mathbf{E}_o \times \mathbf{H}_o \langle \cos^2(\mathbf{k} \cdot \mathbf{x} - \omega t) \rangle_{\mathcal{T}} = \frac{1}{2} \mathbf{E}_o \times \mathbf{H}_o, \tag{3.6}$$

leading to the definition of the *irradiance*

$$I \stackrel{\text{def}}{=} \langle \|\mathbf{S}\| \rangle_{\mathcal{T}} = \frac{1}{2} \|\mathbf{E}_o \times \mathbf{H}_o\| = \frac{1}{2} \sqrt{\frac{\epsilon_o}{\mu_o}} \|\mathbf{E}_o\|^2. \tag{3.7}$$

Thus, the power flow is proportional to the square of the amplitude of the electric field.

### 3.6. Reflection and absorption of power-Fresnel relations

We consider a plane harmonic wave incident upon a plane boundary separating two different materials, specifically vacuum and surface, which produces a reflected wave and an absorbed (refracted) wave (Fig. 2). Two cases for the electric field vector are considered:

- (1) electric field vectors that are parallel ( $\parallel$ ) to the plane of incidence and
- (2) electric field vectors that are perpendicular ( $\perp$ ) to the plane of incidence.

In either case, the tangential components of the electric and magnetic fields are required to be continuous across the interface. Consider case (1). We have the following general vectorial representations

$$\mathbf{E}_{\parallel} = E_{\parallel} \cos(\mathbf{k} \cdot \mathbf{x} - \omega t) \mathbf{e}_1 \quad \text{and} \quad \mathbf{H}_{\parallel} = H_{\parallel} \cos(\mathbf{k} \cdot \mathbf{x} - \omega t) \mathbf{e}_2, \tag{3.8}$$

where  $\mathbf{e}_1$  and  $\mathbf{e}_2$  are orthogonal to the propagation direction  $\mathbf{k}$ . By employing the law of refraction ( $n_i \sin \theta_i = n_a \sin \theta_a$ ) we obtain the following conditions relating the incident, reflected and absorbed components of the electric field quantities

$$E_{\parallel i} \cos \theta_i - E_{\parallel r} \cos \theta_r = E_{\parallel a} \cos \theta_a \quad \text{and} \quad H_{\perp i} + H_{\perp r} = H_{\perp a}. \tag{3.9}$$

Since, for plane harmonic waves, the magnetic and electric field amplitudes are related by  $H = \frac{E}{v\mu}$ , we have

$$E_{\parallel i} + E_{\parallel r} = \frac{\mu_i v_i}{\mu_a v_a} E_{\parallel a} = \frac{\mu_i n_a}{\mu_a n_i} E_{\parallel a} \stackrel{\text{def}}{=} \frac{\hat{n}}{\hat{\mu}} E_{\parallel a}, \tag{3.10}$$

<sup>3</sup> By combining the relations in Eq. (3.5) one obtains  $\|\mathbf{k}\| = \frac{\omega}{c}$ .

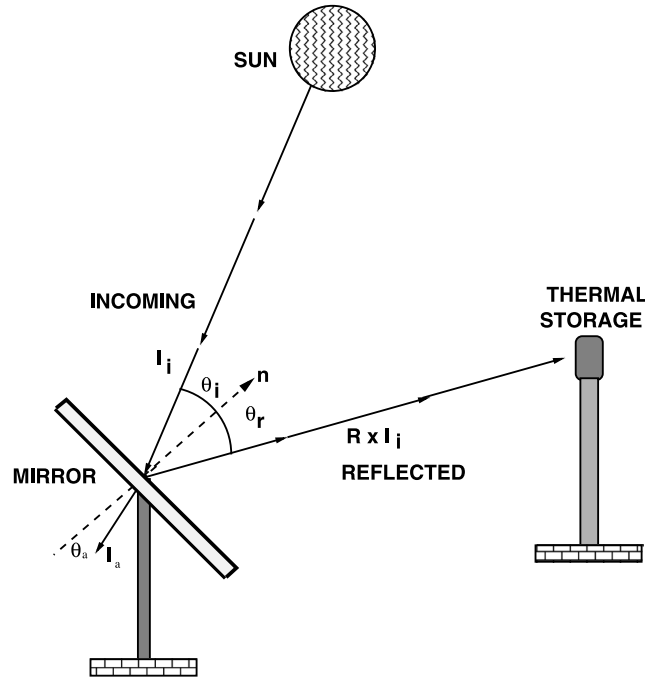


Fig. 2. A single mirror and reflection nomenclature.

where  $\hat{\mu} \stackrel{\text{def}}{=} \frac{\mu_a}{\mu_i}$ ,  $\hat{n} \stackrel{\text{def}}{=} \frac{n_a}{n_i}$  and where  $v_i$ ,  $v_r$  and  $v_a$  are the values of the velocity in the incident, reflected and absorbed directions.<sup>4</sup> By again employing the law of refraction, we obtain the Fresnel reflection and transmission/absorption coefficients, generalized for the case of unequal magnetic permeabilities

$$r_{\parallel} = \frac{E_{\parallel r}}{E_{\parallel i}} = \frac{\frac{\hat{n}}{\mu} \cos\theta_i - \cos\theta_a}{\frac{\hat{n}}{\mu} \cos\theta_i + \cos\theta_a} \quad \text{and} \quad a_{\parallel} = \frac{E_{\parallel a}}{E_{\parallel i}} = \frac{2\cos\theta_i}{\cos\theta_a + \frac{\hat{n}}{\mu} \cos\theta_i}. \tag{3.11}$$

Following the same procedure for case (2), where the components of  $E$  are perpendicular to the plane of incidence, we have

$$r_{\perp} = \frac{E_{\perp r}}{E_{\perp i}} = \frac{\cos\theta_i - \frac{\hat{n}}{\mu} \cos\theta_a}{\cos\theta_i + \frac{\hat{n}}{\mu} \cos\theta_a} \quad \text{and} \quad a_{\perp} = \frac{E_{\perp a}}{E_{\perp i}} = \frac{2\cos\theta_i}{\cos\theta_i + \frac{\hat{n}}{\mu} \cos\theta_a}. \tag{3.12}$$

Our primary interest is in the reflections. We define the reflectances as

$$\mathcal{R}_{\parallel} \stackrel{\text{def}}{=} r_{\parallel}^2 \quad \text{and} \quad \mathcal{R}_{\perp} \stackrel{\text{def}}{=} r_{\perp}^2. \tag{3.13}$$

Particularly convenient forms for the reflections are

$$r_{\parallel} = \frac{\frac{\hat{n}^2}{\mu} \cos\theta_i - (\hat{n}^2 - \sin^2\theta_i)^{\frac{1}{2}}}{\frac{\hat{n}^2}{\mu} \cos\theta_i + (\hat{n}^2 - \sin^2\theta_i)^{\frac{1}{2}}} \quad \text{and} \quad r_{\perp} = \frac{\cos\theta_i - \frac{1}{\mu} (\hat{n}^2 - \sin^2\theta_i)^{\frac{1}{2}}}{\cos\theta_i + \frac{1}{\mu} (\hat{n}^2 - \sin^2\theta_i)^{\frac{1}{2}}}. \tag{3.14}$$

Thus, the total power reflected can be characterized by

$$\mathcal{R} \stackrel{\text{def}}{=} \left( \frac{E_r}{E_i} \right)^2 = \frac{E_{\perp r}^2 + E_{\parallel r}^2}{E_i^2} = \frac{I_{\parallel r} + I_{\perp r}}{I_i}. \tag{3.15}$$

If the resultant plane of oscillation of the (polarized) wave makes an angle of  $\gamma_i$  with the plane of incidence, then

$$E_{\parallel i} = E_i \cos\gamma_i \quad \text{and} \quad E_{\perp i} = E_i \sin\gamma_i, \tag{3.16}$$

<sup>4</sup> Throughout the analysis we assume that  $\hat{n} \geq 1$ .

and it follows from the previous definition of  $I$  that

$$I_{\parallel i} = I_i \cos^2 \gamma_i \quad \text{and} \quad I_{\perp i} = I_i \sin^2 \gamma_i. \tag{3.17}$$

Substituting these expressions back into the equations for the reflectances yields

$$\mathcal{R} = \frac{I_{\parallel r}}{I_i} \cos^2 \gamma_i + \frac{I_{\perp r}}{I_i} \sin^2 \gamma_i = \mathcal{R}_{\parallel} \cos^2 \gamma_i + \mathcal{R}_{\perp} \sin^2 \gamma_i. \tag{3.18}$$

For natural or unpolarized electromagnetic radiation, the angle  $\gamma_i$  varies rapidly in a random manner, as does the field amplitude. Thus, since

$$\langle \cos^2 \gamma_i(t) \rangle_{\mathcal{T}} = \frac{1}{2} \quad \text{and} \quad \langle \sin^2 \gamma_i(t) \rangle_{\mathcal{T}} = \frac{1}{2}, \tag{3.19}$$

and therefore for natural electromagnetic radiation

$$I_{\parallel i} = \frac{I_i}{2} \quad \text{and} \quad I_{\perp i} = \frac{I_i}{2}. \tag{3.20}$$

and therefore

$$r_{\parallel}^2 = \left( \frac{E_{\parallel r}^2}{E_{\parallel i}^2} \right)^2 = \frac{I_{\parallel r}}{I_{\parallel i}} \quad \text{and} \quad r_{\perp}^2 = \left( \frac{E_{\perp r}^2}{E_{\perp i}^2} \right)^2 = \frac{I_{\perp r}}{I_{\perp i}}. \tag{3.21}$$

Thus, the total reflectance becomes

$$\mathcal{R} = \frac{1}{2} (\mathcal{R}_{\parallel} + \mathcal{R}_{\perp}) = \frac{1}{2} (r_{\parallel}^2 + r_{\perp}^2), \tag{3.22}$$

where  $0 \leq \mathcal{R} \leq 1$ . For the cases where  $\sin \theta_a = \frac{\sin \theta_i}{\hat{n}} > 1$ , one may rewrite reflection relations as

$$r_{\parallel} = \frac{\frac{\hat{n}^2}{\hat{\mu}} \cos \theta_i - j (\sin^2 \theta_i - \hat{n}^2)^{\frac{1}{2}}}{\frac{\hat{n}^2}{\hat{\mu}} \cos \theta_i + j (\sin^2 \theta_i - \hat{n}^2)^{\frac{1}{2}}} \quad \text{and} \quad r_{\perp} = \frac{\cos \theta_i - \frac{1}{\hat{\mu}} j (\sin^2 \theta_i - \hat{n}^2)^{\frac{1}{2}}}{\cos \theta_i + \frac{1}{\hat{\mu}} j (\sin^2 \theta_i - \hat{n}^2)^{\frac{1}{2}}}, \tag{3.23}$$

where,  $j = \sqrt{-1}$ , and in this complex case<sup>5</sup>

$$\mathcal{R}_{\parallel} \stackrel{\text{def}}{=} r_{\parallel} \bar{r}_{\parallel} = 1, \quad \text{and} \quad \mathcal{R}_{\perp} \stackrel{\text{def}}{=} r_{\perp} \bar{r}_{\perp} = 1, \tag{3.24}$$

where  $\bar{r}_{\parallel}$  and  $\bar{r}_{\perp}$  are complex conjugates. Thus, for angles above the critical angle  $\theta_i^*$ , all of the power is reflected. Notice that as  $\hat{n} \rightarrow 1$  we have complete absorption, while as  $\hat{n} \rightarrow \infty$  we have complete reflection. The amount of absorbed irradiance by the surface is  $I_a = (1 - \mathcal{R})I_i$ .

### 3.7. Reflectivity

To observe the dependency of  $\mathcal{R}$  on  $\hat{n}$  and  $\theta_i$  we can explicitly write

$$\mathcal{R} = \frac{1}{2} \left( \left( \frac{\frac{\hat{n}^2}{\hat{\mu}} \cos \theta_i - (\hat{n}^2 - \sin^2 \theta_i)^{\frac{1}{2}}}{\frac{\hat{n}^2}{\hat{\mu}} \cos \theta_i + (\hat{n}^2 - \sin^2 \theta_i)^{\frac{1}{2}}} \right)^2 + \left( \frac{\cos \theta_i - \frac{1}{\hat{\mu}} (\hat{n}^2 - \sin^2 \theta_i)^{\frac{1}{2}}}{\cos \theta_i + \frac{1}{\hat{\mu}} (\hat{n}^2 - \sin^2 \theta_i)^{\frac{1}{2}}} \right)^2 \right). \tag{3.25}$$

We observe:

- As  $\hat{n} \rightarrow \infty$ ,  $\mathcal{R} \rightarrow 1$ , no matter what the angle of incidence's value. We note that as  $\hat{n} \rightarrow 1$ , provided that  $\hat{\mu} = 1$ ,  $\mathcal{R} \rightarrow 0$ , i.e. all incident power is absorbed (it is transparent).
- With increasing  $\hat{n}$ , the angle for minimum reflectance grows larger. As mentioned previously, for the remainder of the work, we shall take  $\hat{\mu} = 1$  ( $\mu_o = \mu_i = \mu_a$ ), thus

$$\hat{n} = \frac{n_a}{n_i} = \sqrt{\frac{\epsilon_a \mu_a}{\epsilon_i \mu_i}} \Rightarrow \epsilon_a \mu_a = (\hat{n})^2 \epsilon_i \mu_i \Rightarrow \epsilon_a = (\hat{n})^2 \epsilon_i. \tag{3.26}$$

<sup>5</sup> The limiting case  $\frac{\sin \theta_i^*}{\hat{n}} = 1$ , is the critical angle ( $\theta_i^*$ ) case.

- The previous assumption yields

$$\mathcal{R} = \frac{I_r}{I_i} = \frac{1}{2} \left( \left( \frac{\hat{n}^2 \cos \theta_i - (\hat{n}^2 - \sin^2 \theta_i)^{\frac{1}{2}}}{\hat{n}^2 \cos \theta_i + (\hat{n}^2 - \sin^2 \theta_i)^{\frac{1}{2}}} \right)^2 + \left( \frac{\cos \theta_i - (\hat{n}^2 - \sin^2 \theta_i)^{\frac{1}{2}}}{\cos \theta_i + (\hat{n}^2 - \sin^2 \theta_i)^{\frac{1}{2}}} \right)^2 \right). \tag{3.27}$$

**Remark 3.** Recall that  $\bar{I}$  is the power per unit area, and that we obtain the power associated with an entire pulse/beam by multiplying the irradiance by the area of the mirror,  $\bar{I}A^m$ . The reflection relation, Eq. (3.25), can then be used to compute changes in the magnitude of the reflected rays (and the amount absorbed), with directional changes given by the laws of reflection. We refer the reader to Gross [37] and Zohdi [30–36] for details. We have the following additional observations:

- The angle between the point of contact of a ray (Fig. 2) and the outward normal to the surface at that point is the angle of incidence,  $\theta_i$ . The classical reflection law states that the angle at which a ray is reflected is the same as the angle of incidence and that the incoming (incident,  $\theta_i$ ) and outgoing (reflected,  $\theta_r$ ) ray lays in the same plane, and  $\theta_i = \theta_r$ .
- The classical refraction law states that, if the ray passes from one medium into a second one (with a different index of refraction) and, if the index of refraction of the second medium is less than that of the first, the angle the ray makes with the normal to the interface is always less than the angle of incidence, where  $\hat{n} \stackrel{\text{def}}{=} \frac{v_i}{v_a} = \sqrt{\frac{\epsilon_a \mu_a}{\epsilon_i \mu_i}} = \frac{\sin \theta_i}{\sin \theta_a}$ ,  $\theta_a$  being the angle of the absorbed ray (Fig. 2).

#### 4. Thermal storage and transmission

##### 4.1. Model for the optical receiver

Consider the following power equation for the receiver

$$\underbrace{M_r C_r \frac{dT_r}{dt}}_{\text{stored power}} = \underbrace{\sum_{i=1}^{N_m} \mathcal{R}_i S A_i \eta^{pump}}_{\text{absorbed power}} - \underbrace{\epsilon_r \sigma_r (T_r^4 - T_e^4) A_r}_{\text{radiated power}} - \sum_{c=1}^C F_{rb \rightarrow tgc}^{trans} \stackrel{\text{def}}{=} L_r(t), \tag{4.1}$$

where  $T_r$  is the temperature of the storage system,  $T_e$  is the temperature of the surrounding environment,  $M_r C_r$  is the (lumped) effective “thermal mass” of the system,  $\mathcal{R}_i$  is the effective reflectivity of mirror  $i$ ,  $\bar{I}_i = S$  is the radiant energy from the Sun,  $A_r$  is the system surface area,  $\epsilon_r$  is the radiative emissivity,  $\beta$  is the Stefan–Boltzmann constant and  $F_{rb \rightarrow tgc}^{trans}$  is the transmitted power from the receiver base to the turbine-generator-customer system. This stored power is ready to be accessed by the turbine-generator-customer subsystem.

##### 4.2. Model for the devices (“customers”) in the system

For each device in the system,  $c = 1, 2, \dots, N_c$  (Fig. 1), consider a control volume tracking its energy state. Each device’s energy state (Joules) at time  $t$ , is denoted  $D_c(t)$  and equal to the device state.

- The transmission of energy is governed by the demand of each customer, for example  $D_c^*(t)$ , subject to the following equation and conditions:

$$\frac{dD_c}{dt} = \mathcal{L}_c(t) + F_{rb \rightarrow tgc}^{del} \stackrel{\text{def}}{=} L_c(t), \tag{4.2}$$

where one can assign  $D_c(t) = m_c C_c T_c(t)$ , although this is not absolutely necessary.

- TRANSFER: If  $D_c(t) < D_c^*(t)$ , then  $F_{rb \leftrightarrow tgc} > 0$ , where we wish to induce

$$D_c(t + \Delta t) = D_c^*(t + \Delta t) = D_c(t) + \mathcal{L}_c(t) \Delta t + F_{rb \rightarrow tgc}^{del} \Delta t, \tag{4.3}$$

where  $\mathcal{L}_c$  is the load (losses) carried by device, where the following must be delivered, compensated transmission:

$$F_{rb \leftrightarrow tgc}^{del} = F_{rb \leftrightarrow tgc}^{tran} \alpha_{rc} \alpha_{tg} = \frac{D_c^*(t + \Delta t) - D_c(t)}{\Delta t} - \mathcal{L}_c(t), \tag{4.4}$$

where  $\alpha_{rb \rightarrow c} = e^{-\kappa d_{tg \rightarrow cb}} e^{-\kappa d_{tgc \rightarrow c}}$ , where  $\kappa$  is the power loss per unit length,  $d_{tg \rightarrow cb}$  is the distance between tg and cb,  $d_{cb \rightarrow c}$  is the distance between cb and c and  $0 \leq \alpha_{tg} \leq 1$  is the efficiency of the turbine-generator system. Thus, the actual amount transmitted must be

$$F_{rb \leftrightarrow tgc}^{tran} = \frac{F_{rb \leftrightarrow tgc}^{del}}{\alpha_{rc} \alpha_{tg}}. \quad (4.5)$$

- NO TRANSFER: If  $D_c(t) \geq D_c^*(t)$ , then  $F_{r \leftrightarrow c}^{tran} = 0$ .
- The loss between them is

$$\mathcal{L}_{rb \rightarrow tgc} = F_{rb \rightarrow tgc}^{trans} - F_{rb \rightarrow tgc}^{del} = F_{rb \rightarrow tgc}^{trans} (1 - \alpha_{rb \rightarrow c} \alpha_{tg}). \quad (4.6)$$

### 4.3. The system states

For each customer device:

$$D_c(t + \Delta t) = D_c(t) + \Delta t L_c(t) \approx D_c^*(t + \Delta t) \quad (4.7)$$

and for the receiver

$$T_r(t + \Delta t) = T_r(t) + \frac{\Delta t}{M_r C_r} L_r(t), \quad (4.8)$$

where the received energy is  $E_r = M_r C_r T_r$ .

## 5. Operating temperature optimality

The optimal operating temperature for the thermal storage facility must balance increasing the temperature (and thus thermal storage) with radiative losses to the surroundings. The optimal temperature can be ascertained by optimizing the overall operating efficiency,  $\eta^{overall} = \eta^{csp} \eta^{carnot}$ , computed by comparing the incident optical power ( $P^{inc}$ ) and the amount that is lost ( $P^{lost}$ ):

$$\eta^{csp} = \frac{P^{inc} - P^{lost}}{P^{lost}}, \quad (5.1)$$

where  $P^{inc} = \mathcal{R} \eta^{conver} S N_m A_m$ , where, for this calculation we assume the best possible mirror reflectivity,  $\mathcal{R} = 1$ ,  $0 \leq \eta^{conver} \leq 1$  is the efficiency of conversion incident energy at the receiver,  $S$  is the solar power per unit area,  $N_m$  is the number of mirrors and  $A_m$  is the area of a mirror,  $P_r^{lost} = A_r \epsilon_r \beta (T_r^4 - T_e^4)$ , where  $A_r$  is the surface area of the receiver relative to the theoretical limit of efficiency is the classical Carnot efficiency

$$\eta^{carnot} = \frac{T_r^{hot} - T_e^{cold}}{T_r^{hot}} = \frac{T_r - T_e}{T_r} \quad (5.2)$$

Thus,

$$\eta^{overall} = \eta^{csp} \eta^{carnot} = \left( \frac{P_r^{inc} - P_r^{lost}}{P_r^{lost}} \right) \left( \frac{T_r - T_e}{T_r} \right). \quad (5.3)$$

Inserting the expressions yields:

$$\eta^{overall} = \left( 1 - \frac{A_r \epsilon_r \beta (T_r^4 - T_e^4) + (1 - \eta^{conver}) S N_m A_m}{S N_m A_m} \right) \left( \frac{T_r - T_e}{T_r} \right). \quad (5.4)$$

Assuming  $\eta^{conver} \neq \mathcal{F}(T_r)$ , and taking a derivative

$$\frac{\partial \eta^{overall}}{\partial T_r} = 0 = -4k_1 T_r^3 \left( 1 - \frac{T_e}{T_r} \right) + (\eta^{conver} - k_1 (T_r^4 - T_e^4)) \frac{T_e}{T_r^2}, \quad (5.5)$$

where  $k_1 = \frac{A_r \epsilon_r \beta}{S N_m A_m}$ . This leads to a 5th order polynomial which can be solved easily with Newton's method.

## 6. Power flow-storage-distribution tracking algorithm

Starting at  $t = 0$  and ending at  $t = t^{lim}$ , algorithmically, the overall system operates in the following manner:

1. Optical energy flows from the sun to the mirrors,
2. Mirrors orient themselves to reflect light towards the thermal storage system (there are reflective losses and tracking motor losses),
3. The optical receiver (thermal storage system) absorbs energy and stores it (thermal radiation losses),
4. A turbine-generator system produces electricity for customers on demand (producing thermo-mechanical losses and transmission losses),
5. Customers induce individual loads on the system that lead to losses.

## 7. Machine-learning optimization and automatic design

A design vector of the form  $\Lambda^i \stackrel{\text{def}}{=} \{\Lambda_1^i, \Lambda_2^i, \dots, \Lambda_N^i\} = \{\text{solar farm size, solar farm shape, received height, thermal storage fluid properties, mirror sizes, mirror numbers, customer access periods}\}$  and cost-error function of the following form

$$\begin{aligned} \Pi(\Lambda) = & W_1 \times (\text{customer demand shortfall}) + W_2 \times (\text{customer storage excess}) \\ & + W_3 \times (\text{receiver storage shortfall}) + W_4 \times (\text{receiver storage excess}) \\ & + W_5 \times (\text{tracking motor energy}), \end{aligned} \quad (7.1)$$

where we consider a design vector  $\Lambda^i \stackrel{\text{def}}{=} \{\Lambda_1^i, \Lambda_2^i, \Lambda_3^i, \dots, \Lambda_N^i\}$ , which represents the positions of the devices and where the cost is the power integrated over the course of time. Specifically:

- Customer demand shortfall: If  $D_i(t) \leq D_i^*(t)$  then ( $D_i = m_i C_i T_i$ ,  $D_i^* = m_i C_i T_i^*$ ),

$$\Pi_i^{(1)}(t + \Delta t) = \Pi_i^{(1)}(t) + \|D_i(t) - D_i^*(t)\| \text{ and } \Pi_i^{(2)}(t + \Delta t) = \Pi_i^{(2)}(t), \quad (7.2)$$

where  $\Pi^{(1)} = \sum_{i=1}^{N_c} \Pi_i^{(1)}$  and  $\Pi^{(2)} = \sum_{i=1}^{N_c} \Pi_i^{(2)}$ .

- Customer storage excess: If  $D_i(t) > D_i^*(t)$  then

$$\Pi_i^{(1)}(t + \Delta t) = \Pi_i^{(1)}(t) \text{ and } \Pi_i^{(2)}(t + \Delta t) = \Pi_i^{(2)}(t) + \|D_i(t) - D_i^*(t)\|, \quad (7.3)$$

where  $\Pi^{(1)} = \sum_{i=1}^{N_c} \Pi_i^{(1)}$  and  $\Pi^{(2)} = \sum_{i=1}^{N_c} \Pi_i^{(2)}$ .

- Receiver storage shortfall: If  $E_r(t) \leq E_r^*(t)$  then ( $E_r = M_r C_r T_r$ ,  $E_r^* = M_r C_r T_r^*$ ),

$$\Pi^{(3)}(t + \Delta t) = \Pi^{(3)}(t) + \|E_r(t) - E_r^*(t)\| \text{ and } \Pi^{(4)}(t + \Delta t) = \Pi^{(4)}(t). \quad (7.4)$$

- Receiver storage excess: If  $E_r(t) > E_r^*(t)$  then

$$\Pi^{(3)}(t + \Delta t) = \Pi^{(3)}(t) \text{ and } \Pi^{(4)}(t + \Delta t) = \Pi^{(4)}(t) + \|E_r(t) - E_r^*(t)\|. \quad (7.5)$$

- Tracking motors total energy (Fig. 2):

We compute the change in angle for each mirror panel, via an inner-product of the unit normals ( $m = 1, 2, \dots, N_m$  from time  $t$  to  $t + \Delta t$ ),

$$\mathbf{n}_m(t + \Delta t) \cdot \mathbf{n}_m(t) = \cos(\Delta\theta(t)) \Rightarrow \Delta\theta = \cos^{-1}(\mathbf{n}_m(t + \Delta t) \cdot \mathbf{n}_m(t)) \quad (7.6)$$

and compute the power needed

$$\Delta E_m(t) = \alpha_m \|\Delta\theta(t)\| e^{ld_m}, \quad (7.7)$$

where  $\alpha_m$  is the torque multiplier  $\alpha_m = A_m \times 10^6$ , where  $A_m$  is the surface area of the panel,  $e^{ld_m}$  is the compensation for the losses for the power that needs to be supplied to the motor, where  $l$  is a loss coefficient and  $d_m$  is the distance of mirror  $m$  from the power supply (the generator). The motor torque is then computed for each mirror:

$$\Pi_m^{(5)}(t + \Delta t) = \Pi_m^{(5)}(t) + \Delta E_m, \quad (7.8)$$

where  $\Pi^{(5)} = \sum_{i=1}^{N_m} \Pi_i^{(5)}$ .

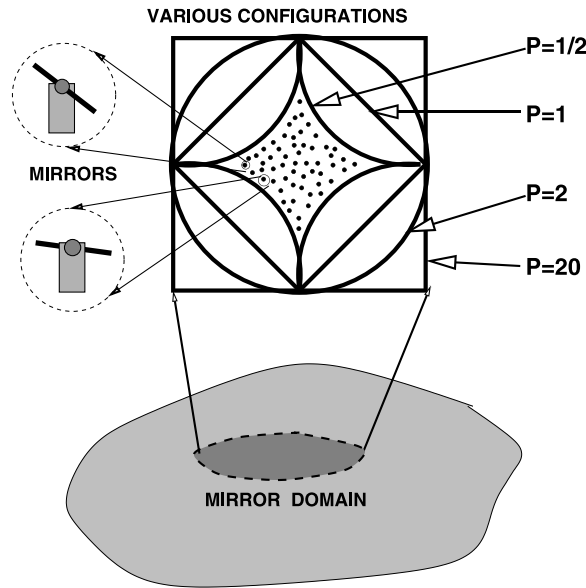


Fig. 3. Possible mirror-domain layouts generated from a generalized 2D-ellipsoidal equation (Eq. (7.10)).

All of these components are then summed up until time= $t = t^f$ , which is the final time, and normalized

$$\Pi^{tot}(t = t^f) = \frac{1}{\Pi^*} \sum_{k=1}^5 \Pi^{(k)}(t^f), \tag{7.9}$$

where  $N_d$  is the number of days and where  $\Pi^* = E_r^* N_d$ , is an energy-based normalizer.

**Note:** One could also compute the capital costs by summing cost per mirror, receiver costs, etc, into the cost function, with the appropriate normalization.

### 7.1. Distribution of mirrors

For the mirror layout, we consider a topology described by the normalized equation for a surface,  $F(x_1, x_2) = 1$  (Fig. 3). Specifically, a generalized 2D-ellipsoidal equation (Eq. (7.10)) is used where, for exponent values of  $(p_1, p_2)$  equal to two, (2, 2), we generate a familiar 2D-ellipsoidal surface, for values less than one we generate involute (nonconvex shapes and corresponding surfaces), and for exponent values of  $(p_1, p_2)$  greater than two, we generate a rectangular-like shapes (Fig. 3). To generate a panel, a generalized 2D-ellipsoidal equation is used

$$F(x_1, x_2) = \left\| \frac{x_1 - x_{1o}}{R_1} \right\|^{p_1} + \left\| \frac{x_2 - x_{2o}}{R_2} \right\|^{p_2} = 1 \tag{7.10}$$

where  $(x_{1o}, x_{2o})$  are the coordinates of the panel center and  $(R_1, R_2)$  are the generalized radii and  $(p_1, p_2)$  are exponents of the generalized 2D-ellipsoid, which ultimately will be design variables in the machine-learning Algorithm discussed later. In order to avoid clustering of the devices, we enforce a spacing penalty for a configuration consisting of a proximity penalization function summing all individual pairwise device separation distances

$$\zeta \stackrel{\text{def}}{=} \frac{\sqrt{\sum_{i=1}^N \sum_{j=1}^N \phi_{ij} (\|r_i - r_j\| - d^*)^2}}{Nd^*}, \tag{7.11}$$

where  $r_i$  is the position vector of device  $i$ ,  $r_j$  is the position vector of device  $j$ ,  $d^*$  is a critical separation distance and where:

- If  $\|r_i - r_j\| \leq d^*$  then  $\phi_{ij} = 1$ ,
- If  $\|r_i - r_j\| > d^*$  then  $\phi_{ij} = 0$ .

This ensures a uniform distribution of mirrors. An example of a distribution of mirrors in a  $\{p_1, p_2\} = \{0.75, 0.75\}$  domain is shown in Fig. 4. The rapid rate at which these simulations can be completed allows the exploration of inverse problems seeking to determine what parameter combinations can deliver a desired result (Fig. 5). In order to cast the objective mathematically, we set the problem up as a machine-learning algorithm (MLA), specifically a genetic algorithm (GA) variant, which is well-suited for nonconvex optimization. Following Zohdi [1,29,39–44], we formulate the objective as a cost function minimization problem that seeks system parameters that match a desired response, in this case a minimum of  $\Pi(\Lambda_1, \dots, \Lambda_N)$ . We systematically minimize  $\Pi$ , by varying the design parameters:  $\Lambda^J \stackrel{\text{def}}{=} \{\Lambda_1^J, \Lambda_2^J, \Lambda_3^J, \dots, \Lambda_N^J\}$ . The system parameter search is conducted within the constrained ranges of  $\Lambda_1^{(-)} \leq \Lambda_1 \leq \Lambda_1^{(+)}$ ,  $\Lambda_2^{(-)} \leq \Lambda_2 \leq \Lambda_2^{(+)}$ ,  $\Lambda_3^{(-)} \leq \Lambda_3 \leq \Lambda_3^{(+)}$ , etc. These upper and lower limits are dictated by what is physically feasible.

## 7.2. Machine-learning algorithm (MLA)

Cost functions such as  $\Pi$  are nonconvex in design parameter space and often nonsmooth. Their minimization is usually difficult with direct application of gradient-based methods. This motivates nonderivative search methods, for example those found in machine-learning algorithms (MLAs). One of the most basic subsets of MLAs are so-called Genetic Algorithms (GAs). For a review of GAs, see the pioneering work of John Holland ([45], [46]), as well as Goldberg [47], Davis [48], Onwubiko [49] and Goldberg and Deb [50]. A description of the algorithm will be described next, following Zohdi [1,29,39–44].

## 7.3. Algorithmic structure

The MLA/GA approach is extremely well-suited for nonconvex, nonsmooth, multicomponent, multistage systems and, broadly speaking, involves the following essential concepts (Fig. 5):

- 
1. **POPULATION GENERATION:** Generate a parameter population of genetic strings:  $\Lambda^i$
  2. **PERFORMANCE EVALUATION:** Compute performance of each genetic string:  $\Pi(\Lambda^i)$
  3. **RANK STRINGS:** Rank them  $\Lambda^i$ ,  $i = 1, \dots, S$  from best to worst
  4. **MATING PROCESS:** Mate pairs/produce offspring
  5. **GENE ELIMINATION:** Eliminate poorly performing genetic strings
  6. **POPULATION REGENERATION:** Repeat process with updated gene pool and new *random* genetic strings
  7. **SOLUTION POST-PROCESSING:** Employ gradient-based methods afterwards in local “valleys”-if *smooth enough*
- 

## 7.4. Specifics

Following Zohdi [1,29,39–44], the algorithm is as follows:

- **STEP 1:** Randomly generate a population of  $S$  starting genetic strings,  $\Lambda^i (i = 1, 2, 3, \dots, S)$  :

$$\Lambda^i \stackrel{\text{def}}{=} \left\{ \begin{array}{c} \Lambda_1^i \\ \Lambda_2^i \\ \Lambda_3^i \\ \dots \\ \Lambda_N^i \end{array} \right\} \quad (7.12)$$

- **STEP 2:** Compute fitness of each string  $\Pi(\Lambda^i)$ , ( $i=1, \dots, S$ )
- **STEP 3:** Rank genetic strings:  $\Lambda^i$ , ( $i=1, \dots, S$ ) from best to worst

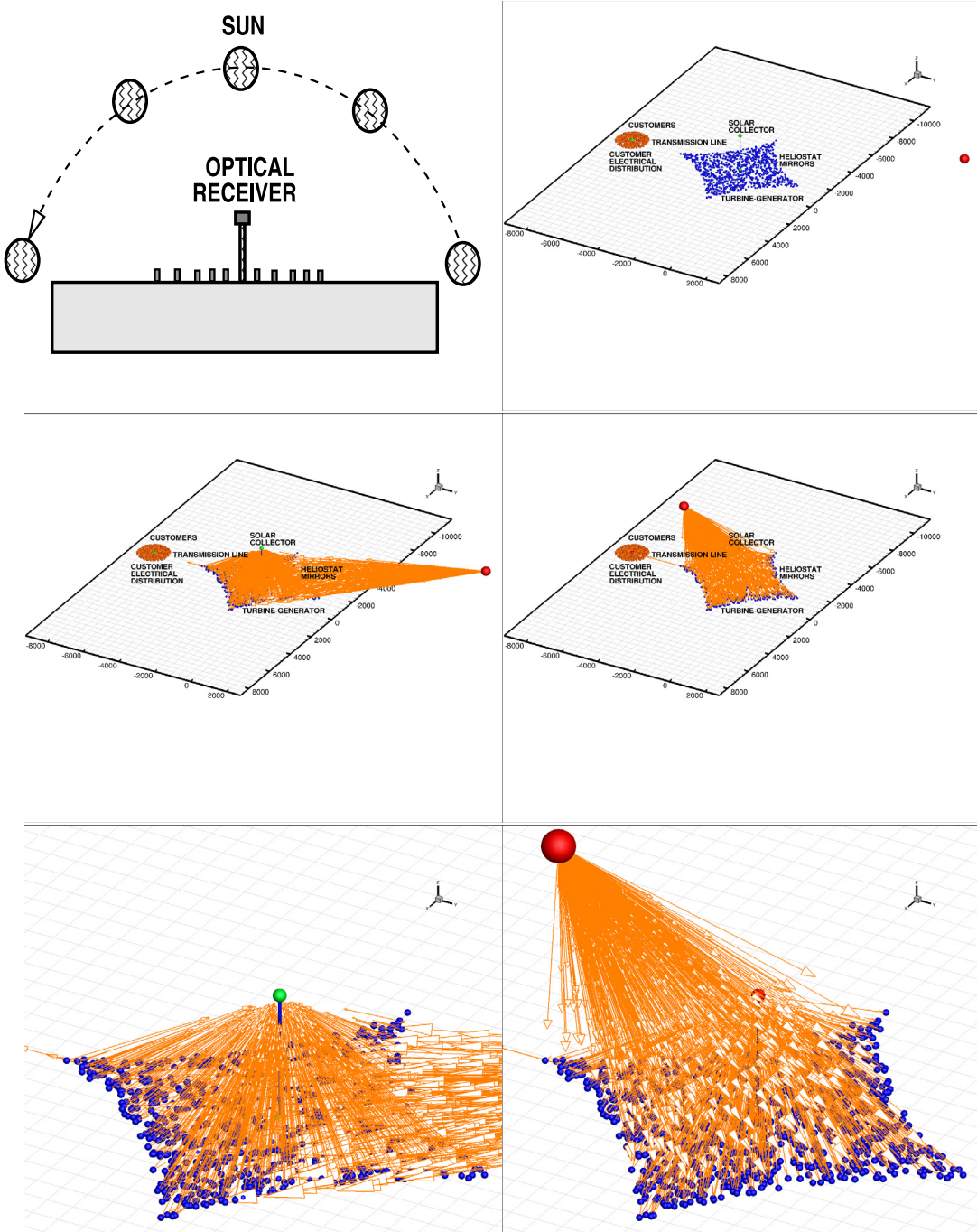


**Fig. 4.** The overall system for one day. A 365 day simulation (365 day cycles) takes on the order of 0.25 s. From left to right and top to bottom: Frame 1 (top left): A schematic of a “day”. Frame 2 (top right): An example of a simulation configuration. Frame 3 (middle left): The start of the day at “dawn”, with light vectors. Frame 4 (middle right): Mid-day with light vectors. Frame 5 (bottom left): A zoom on the start of the day at “dawn”. Frame 6 (bottom right): A zoom on the mid-day.

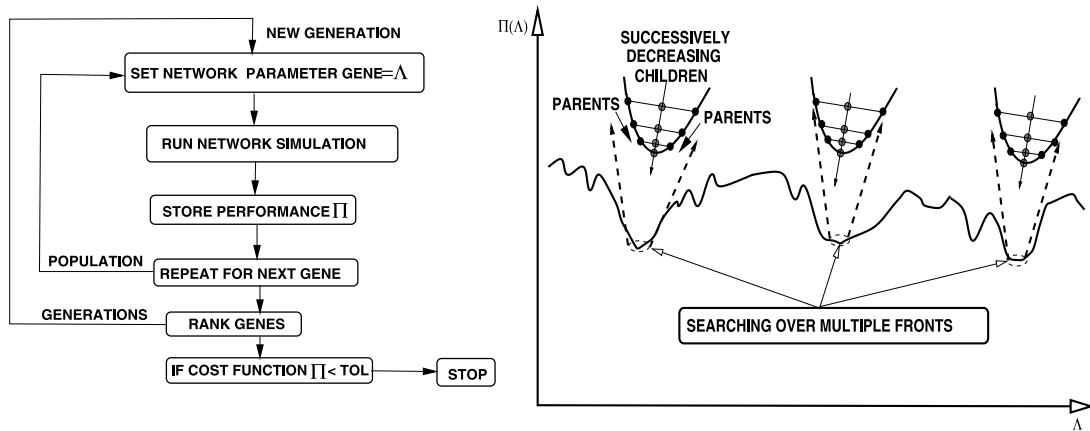


Fig. 5. The basic action of a machine-learning/genetic algorithm (Zohdi [1,29,39–44]) inducing multidirectional search.

- **STEP 4:** Mate nearest pairs and produce two offspring, (i=1, ..., S):

$$\lambda^i \stackrel{\text{def}}{=} \Phi \circ \Lambda^i + (1 - \Phi) \circ \Lambda^{i+1} \stackrel{\text{def}}{=} \begin{Bmatrix} \phi_1 \Lambda_1^i \\ \phi_2 \Lambda_2^i \\ \phi_3 \Lambda_3^i \\ \dots \\ \phi_N \Lambda_N^i \end{Bmatrix} + \begin{Bmatrix} (1 - \phi_1) \Lambda_1^{i+1} \\ (1 - \phi_2) \Lambda_2^{i+1} \\ (1 - \phi_3) \Lambda_3^{i+1} \\ \dots \\ (1 - \phi_N) \Lambda_N^{i+1} \end{Bmatrix} \quad (7.13)$$

and

$$\lambda^{i+1} \stackrel{\text{def}}{=} \Psi \circ \Lambda^i + (1 - \Psi) \circ \Lambda^{i+1} \stackrel{\text{def}}{=} \begin{Bmatrix} \psi_1 \Lambda_1^i \\ \psi_2 \Lambda_2^i \\ \psi_3 \Lambda_3^i \\ \dots \\ \psi_N \Lambda_N^i \end{Bmatrix} + \begin{Bmatrix} (1 - \psi_1) \Lambda_1^{i+1} \\ (1 - \psi_2) \Lambda_2^{i+1} \\ (1 - \psi_3) \Lambda_3^{i+1} \\ \dots \\ (1 - \psi_N) \Lambda_N^{i+1} \end{Bmatrix} \quad (7.14)$$

where for this operation, the  $\phi_j$  and  $\psi_j$  are random numbers, such that  $0 \leq \phi_j \leq 1$ ,  $0 \leq \psi_j \leq 1$ , ( $j = 1, 2, \dots, N$ ) which are different for each component of each genetic string

- **STEP 5:** Eliminate the bottom  $M$  strings and keep top  $K$  parents and their  $K$  offspring ( $K$  offspring+ $K$  parents+ $M=S$ )
- **STEP 6:** Repeat STEPS 1–5 with top gene pool ( $K$  offspring and  $K$  parents), plus  $M$  new, randomly generated, strings
- **REFOCUS OPTION:** One can refocus search around best performing parameter set every few generations, thus concentrating the computation effort around the most promising (optimal) areas of design space.

**Remark 4.** If one selects the mating parameters  $\phi$ 's and  $\psi$ 's to be greater than one and/or less than zero, one can induce “mutations”, i.e. characteristics that neither parent possesses. However, this is somewhat redundant with introduction of new random members of the population in the current algorithm. If one does not retain the parents in the algorithm above, it is possible that inferior performing offspring may replace superior parents. Thus, top parents should be kept for the next generation. This guarantees a monotone reduction in the cost function, unless one implements the refocussing option mentioned previously. Retained parents do not need to be reevaluated, making the algorithm less computationally expensive, since these parameter sets do not have to be reevaluated in the next generation's calculations. In the absence of refocussing, numerous studies of the author (Zohdi [1,29,39–44]) have shown that the advantages of parent retention outweighs inbreeding, for sufficiently large population sizes. Finally, we observe that this algorithm is easy to parallelize.

**Remark 5.** After application of such a global search algorithm, one can apply a gradient-based method around the best performing parameter set, if the objective function is sufficiently smooth in that region of the parameter space. In other words, if one has located a convex portion of the parameter space with a global genetic search, one can employ gradient-based procedures locally to minimize the objective function further, since they are generally much more efficient for convex optimization of smooth functions. An exhaustive review of these methods can be found in the texts of Luenberger [51] and Gill, Murray and Wright [52]. *However, refocussing usually makes this extra step unnecessary, since the search eventually concentrates the computational effort locally around the best parameter set beforehand.*

### 7.5. Algorithmic settings

In this example, the following search parameter settings were used:

- Number of design variables: 10,
- Population size per generation: 24,
- Number of parents to keep in each generation: 6,
- Number of children created in each generation: 6,
- Number of completely new genes created in each generation: 12,
- Number of generations for re-adaptation around a new search interval: 10 and
- Number of generations: 150.

The simulation time was 365 days and with 1000 mirrors. The best gene was computed to be

$$\begin{aligned} \mathbf{A}^* &= \{A_1^*, A_2^*, \dots, A_{10}^*\} \\ &= \{0.676, 5107.85, 5627.06, 2.14, 4.50, 130.40, 1.00, 29.52, 1027.99, 2101.29\}, \end{aligned} \quad (7.15)$$

where

- the customer “on” time:  $t^c = A_1$ ,
- the  $x_1$  radius of the mirror field:  $R_1 = A_2$ ,
- the  $x_2$  radius of the mirror field:  $R_2 = A_3$ ,
- the  $x_1$  radius exponent of the mirror field:  $p_1 = A_4$ ,
- the  $x_2$  radius exponent of the mirror field:  $p_2 = A_5$ ,
- the receiver height:  $h = A_6$ ,
- the mirror size:  $L_m = A_7$ ,
- the receiver size,  $L_r = A_8$ ,
- the operating material density:  $\rho_r = A_9$ ,
- the receiver heat capacity:  $C_r = A_{10}$ ,

with a cost function of  $\Pi(\mathbf{A}^*) = 0.089$ . Fig. 6 illustrates the results for the cost function for the best performing gene (*red*) as a function of successive generations, as well as the average performance cost function of the entire population of genes (*green*). We allowed the MLA/GA to readapt every 10 generations. Often, this action is more efficient than allowing the algorithm not to readapt, since it probes around the current optimum for better local alternatives. The total cost (population average) function was initially  $\Pi^{total} \approx 0.1529$  and was reduced to  $\Pi^{tot} \approx 0.0890$ , a reduction of  $\frac{0.1529-0.0890}{0.1529} \rightarrow 41.79\%$ . The entire 150 generation simulation, with 24 genes per evaluation (3600 total designs) took a few minutes on a laptop, *making it ideal as a design tool*. We note that, for a given set of parameters, a complete simulation takes a fraction of a second, thus hundreds of thousands of parameter sets can be evaluated in an hour, *without even exploiting the inherent parallelism of the MLA/GA*. The speed at which the overall process can be completed makes it a suitable digital-twin of the system that can run in real-time or faster than the actual physical system, making it suitable as either a design tool or an adaptive controller.

### 7.6. Simulation acceleration-model reduction via Artificial Neural Nets

There are other machine-learning type paradigms that complement genetic-based approaches, such as Artificial Neural Networks (ANN). ANN have received huge attention in the scientific community over the last decade and

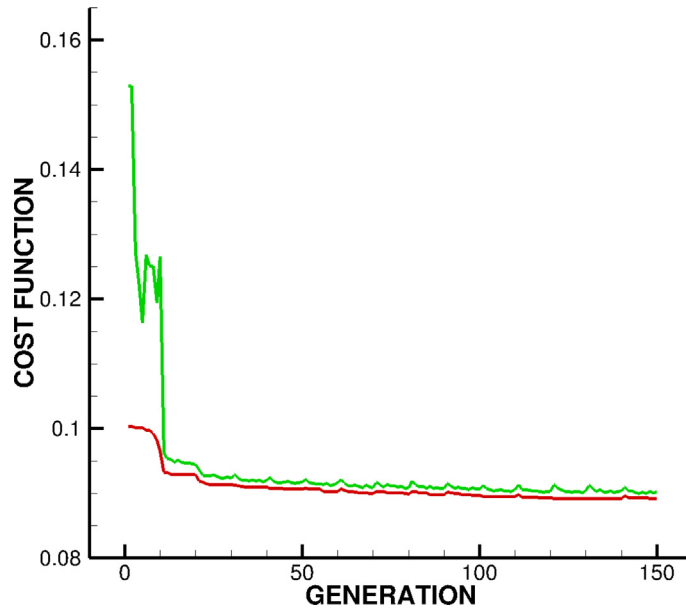


**Fig. 6.** Successive generations. This figure illustrates the results for the cost function for the best performing gene (*red*) as a function of successive generations, as well as the average performance cost function of the entire population of genes (*green*). We allowed the MLA/GA to readapt every 10 generations. Often, this action is more efficient than allowing the algorithm not to readapt, since it probes around the current optimum for better local alternatives. The total cost function was initially  $\Pi^{total} \approx 0.1529$  and was reduced to  $\Pi^{tot} \approx 0.0890$  a reduction of  $\frac{0.1529-0.0890}{0.1529} \rightarrow 41.79\%$ . (For interpretation of the references to color in this figure legend, the reader is referred to the web version of this article.)

are based on layered input–output type frameworks that are essentially adaptive nonlinear regressions of the form  $\mathcal{O} = \mathcal{B}(\mathbf{I}, \mathbf{w})$ , where  $\mathcal{O}$  is a desired output and  $\mathcal{B}$  is the ANN comprised of (1) **synapses**, which multiply inputs ( $I_i, i = 1, 2, \dots, M$ ) by weights ( $w_i, i = 1, 2, \dots, N$ ) that represent the input relevance to the desired output, (2) **neurons**, which aggregate outputs from all incoming synapses and apply activation functions to process the data and (3) **training**, which calibrates the weights to match a desired overall output. This is discussed next and follows a framework developed in Zohdi [53].

### 7.6.1. ANN framework

A primary issue with ANN is the calibration of the synapse weights. This calibration can be cast as a nonconvex optimization problem, whereby the cost/error function represents the normed difference between observed data and the output of the ANN for a selected set of weights. The objective is to select a set of weights which minimizes the cost/error. The genetic-based machine-learning algorithm introduced earlier for the model problem optimization are well-suited to calibrate an ANN, which we illustrate next.

### 7.6.2. ANN construction

ANNs are based on layered input–output type frameworks that are essentially adaptive nonlinear regressions of the form

$$\mathcal{O} = \mathcal{B}(I_1, I_2, \dots, I_M, w_1, w_2, \dots, w_N), \quad (7.16)$$

where  $\mathcal{O}$  is a desired output and  $\mathcal{B}$  is the ANN comprised of:

- **Synapses**, which multiply inputs ( $I_1, I_2, \dots, I_M$ ) by weights ( $w_1, w_2, \dots, w_N$ ) that represent the input relevance to the desired output,
- **Neurons**, which aggregate outputs from all incoming synapses and apply activation functions to process the data and
- **Training**, which calibrates the weights to match a desired overall output.

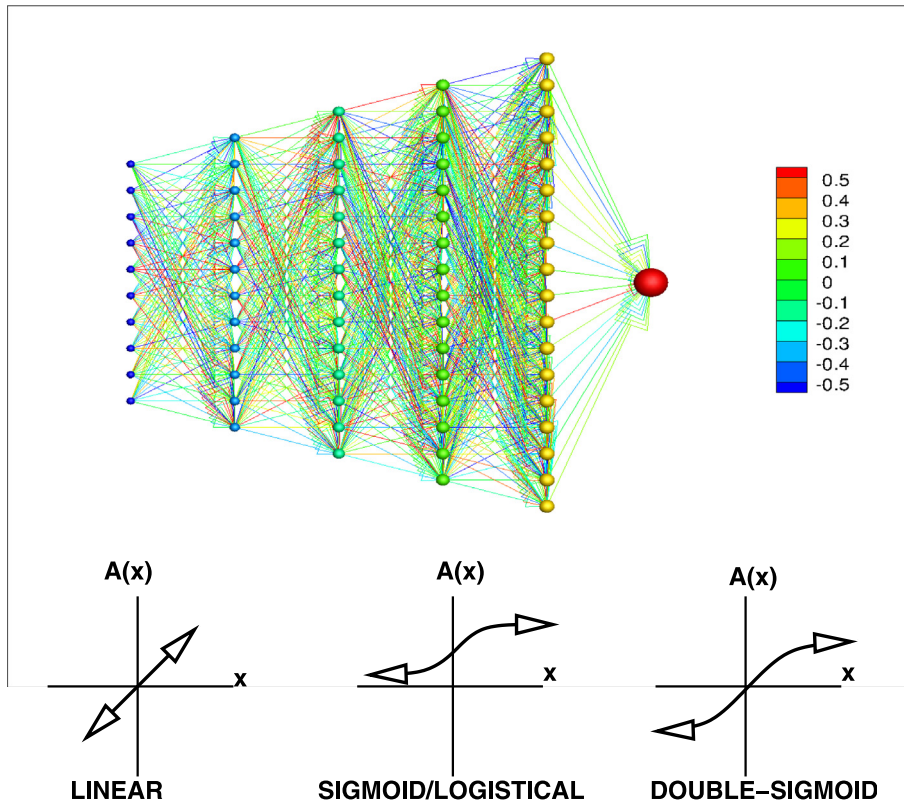


**Fig. 7.** Top: An ANN comprised of (1) Five layers (one input layer and four hidden layers) (2) 70 activation neurons (10+12+14+16+18) and (3)  $10 \times 12 + 12 \times 14 + 14 \times 16 + 16 \times 18 + 18 = 818$  weighted synapses. The color-coding represents the value of the synapse weights. Bottom: Various neuron activation functions: (1) Linear (2) Sigmoid and (3) Double Sigmoid.

For example, Fig. 7 illustrates a detailed ANN comprised of (1) Five layers (one input layer and four hidden layers) (2) 70 activation neurons (10+12+14+16+18) and (3)  $10 \times 12 + 12 \times 14 + 14 \times 16 + 16 \times 18 + 18 = 818$  weighted synapses. *The primary issue with ANNs is the calibration or “training” of the synapse weights.* The key components of an ANN can be summarized as follows (which is centered around training):

- STEP 1: Guess a set of trial weights (trials,  $i = 1, 2, \dots$ ), given by the vector  $w^{i=1}$ , for the synapse weights and insert into the ANN (detailed construction shown shortly)

$$\mathcal{B}(I, w^i) = \mathcal{O}^i, \tag{7.17}$$

which produces an overall trial output (*ith* trial).

- STEP 2: Compute the error for the *ith* trial

$$\mathcal{E}^i \stackrel{\text{def}}{=} \|\mathcal{O}^{\text{desired}} - \mathcal{O}^i\|, \tag{7.18}$$

where  $\mathcal{O}^{\text{desired}}$  is the desired output, which could come from experimental/field data or results from a complex computational model of a system, where a reduced complexity ANN may be useful to represent the system.

- STEP 3: The minimization of the error by adjusting the weights, for the next trial ( $i + 1$ ):

$$\mathbf{w}^{i+1} = \mathbf{w}^i + \Delta \mathbf{w}^i \quad (7.19)$$

- STEP 4: Repeat Steps 1–3 (trials  $i = 1, 2, \dots$ ) until the best set of weights are found to minimize the error.

The determination of the synapse weights can be cast as a nonconvex optimization problem, whereby the cost/error function represents the normed difference between observed data and the output of the ANN for a selected set of weights. The specifics of ANN construction are as follows:

- **Step 1:** Assign initial starting “guessed” weights to the synapses; this is the number of unknowns to be updated/optimized:  $\mathbf{w}^i$ , for trials  $i = 1, 2, \dots$
- **Step 2:** Collect (sum) the input ( $I_k, k = 1, \dots, \text{synapses}$ , Fig. 7) from each synapse input to each neuron:
- Neuron 1:  $I_1 w_{1 \rightarrow N_1} + I_2 w_{2 \rightarrow N_1} + \dots = S_{N_1}$ , Neuron 2:  $I_1 w_{1 \rightarrow N_2} + I_2 w_{2 \rightarrow N_2} + \dots = S_{N_2}$ , etc.
- **Step 3:** For each neuron, apply an activation function (Fig. 7) to process input: Neuron 1:  $A_{N_1}(S_{N_1})$ , Neuron 2:  $A_{N_2}(S_{N_2})$ , etc.
- Linear activation:  $A(x) = x$  which provides proportional feedback
- Sigmoid/logistical activation:  $A(x) = \frac{1}{1+e^{-x}}$ , reinforces input for  $x \rightarrow \infty$  and deletes input for  $x \rightarrow -\infty$
- Double-sigmoid activation:  $A(x) = \frac{1-e^{-x}}{1+e^{-x}}$ , reinforces input for  $x \rightarrow \infty$  and negates input for  $x \rightarrow -\infty$
- **Step 4:** The output function sums contributions from the last layer:

$$\mathcal{O}(\sum_{j=1}^{N_{last}} w_{N_j \rightarrow O} A_{N_j}(S_{N_j})) \stackrel{\text{def}}{=} \mathcal{O}^i. \quad (7.20)$$

- **Step 5:** Compute the error  $\mathcal{E}^i = \|\mathcal{O}^{Desired} - \mathcal{O}^i\|$ , in the appropriate problem specific norm, where  $\mathcal{O}^{Desired}$  is observed data to be matched.
- **Step 6:** Repeat Steps 1–5 with an updated (improved) set of weights until a cost function  $\Pi(\mathbf{A}^i) \stackrel{\text{def}}{=} \mathcal{E}^i$  is minimized by varying a weight vector  $\mathbf{w}^i \stackrel{\text{def}}{=} \{w_1^i, w_2^i, \dots, w_N^i\}$ . This is the key step, referred to as *training* or *calibration*.

### 7.6.3. Calibration via genetic-based machine-learning

The objective now is to minimize the cost function

$$\Pi(w_1^i, \dots, w_N^i) \stackrel{\text{def}}{=} \mathcal{E}^i = \|\mathcal{O}^{Desired} - \mathcal{O}^i\|, \quad (7.21)$$

by varying the weight vector  $\mathbf{w}^i \stackrel{\text{def}}{=} \{w_1^i, w_2^i, w_3^i, \dots, w_N^i\}$ , for repeated trials  $i = 1, 2, \dots$ . In order to cast the objective mathematically, we set the problem up as a genetic-based machine-learning algorithm.

### 7.6.4. Algorithmic structure

As introduced earlier in the work, genetic-based Machine Learning Algorithms are well-suited ANN calibration. To be consistent with the genetic-algorithm terminology, we shall use the term “trial” interchangeably with “generation” and follow the process:

1. **POPULATION GENERATION:** Generate a parameter population  $i = 1, 2, \dots, S$  of genetic strings,  $\mathbf{w}^i$
2. **PERFORMANCE EVALUATION:** Compute performance of each genetic string:  $\Pi(\mathbf{w}^i)$

3. **RANK STRINGS:** Rank them  $\mathbf{w}^i$ ,  $i = 1, 2, \dots, S$  from best to worst
  4. **MATING PROCESS:** Mate pairs/produce offspring
  5. **GENE ELIMINATION:** Eliminate poorly performing genetic strings
  6. **POPULATION REGENERATION:** Repeat process with updated gene pool and new *random* genetic strings
  7. **SOLUTION POST-PROCESSING:** Employ gradient-based methods afterwards in local “valleys”-if *smooth enough*.
- 

### 7.6.5. Example: genetic training of an ANN

As an example, we consider a model problem where synthetic data is developed by repeated simulation of the MLA optimized digital twin introduced earlier. The objective being to reduce the system even further to an input–output “App” that requires no simulations of differential equations afterwards. For example, a user would input the number of days and the output would be the value of the cost function. This makes it ideal for handheld computation in the field.

### 7.6.6. Generation of a synthetic data set, Neural Net configuration and cost function

As an example, we evaluated the system for  $j = 1, 2, \dots, 100$  random  $\mathbf{A}^{solar,j}$  (designs) in order to train the Neural Net. Each “true” system response was labeled as  $\Gamma(\mathbf{A}^{solar,i})$ . These are “synthetic” data points. We used an ANN (Fig. 7) comprised of (1) Five layers (one input layer and four hidden layers) (2) 70 activation neurons ( $10 + 12 + 14 + 16 + 18$ ) and (3)  $10 \times 12 + 12 \times 14 + 14 \times 16 + 16 \times 18 + 18 = 818$  weighted synapses. Our objective is the use of genetic-based machine-learning to calibrate the 818 weights for the synapses. The cost function is

$$\Pi(\mathbf{w}^i) = \sum_{j=1}^{D=100} |\Gamma(\mathbf{A}^{solar,j}) - \mathcal{O}(\mathbf{w}^i, \mathbf{A}^{solar,j})|, \quad (7.22)$$

where  $\mathbf{w}^i$  is the vector of synapse weights to be calibrated with the genetic-based machine-learning algorithm.

### 7.6.7. Algorithmic settings

In the upcoming example:

- Search parameter ranges:  $-1 = w_k^- \leq w_k \leq w_k^+ = 1$  for the  $k = 1, 2, \dots, 818$  synapse weights,
- Number of weight variables: 818,
- Population size per generation: 24,
- Number of parents to keep in each generation: 6,
- Number of children created in each generation: 6,
- Number of completely new genes created in each generation: 12,
- Number of generations for re-adaptation around a new search interval: 20 and
- Number of generations: 50.

A double sigmoid function (Fig. 7) was used. Any advantage of one type of activation function over another, when training with genetic algorithms, is problem specific. Fig. 8 illustrates the one hundred synthetic data points used to train the Neural Net ( $\mathcal{O}^{Desired}$ ). Fig. 9 illustrates the reduction of error by the genetic-Machine Learning Algorithm (best performing gene (red) and the average of the population (green)). Also shown are the values optimized (818) synapse weights that comprise the design vector. The evolution of the best synapse weights stabilized after about 25 generations. From left to right and top to bottom at generations 1, 2, 4, 8, 16 and 32. The ANN is comprised of (1) Five layers (one input layer and four hidden layers) (2) 70 activation neurons ( $10 + 12 + 14 + 16 + 18$ ) and (3)  $10 \times 12 + 12 \times 14 + 14 \times 16 + 16 \times 18 + 18 = 818$  weighted synapses. The color-coding represents the value of the synapse weights. Fig. 10 illustrates the evolution of the best synapse weights, which stabilized after about 25 generations. From left to right and top to bottom at generations 1, 2, 4, 8, 16 and 32. The ANN is comprised of (1) Five layers (one input layer and four hidden layers) (2) 70 activation neurons ( $10 + 12 + 14 + 16 + 18$ ) and (3)  $10 \times 12 + 12 \times 14 + 14 \times 16 + 16 \times 18 + 18 = 818$  weighted synapses. The color-coding represents the value of the synapse weights. The weights were chosen to vary between  $-1$  and  $+1$ , but of course there is nothing stopping choices outside of this range. This was done simply to allow for a clear presentation in the example. The best gene’s

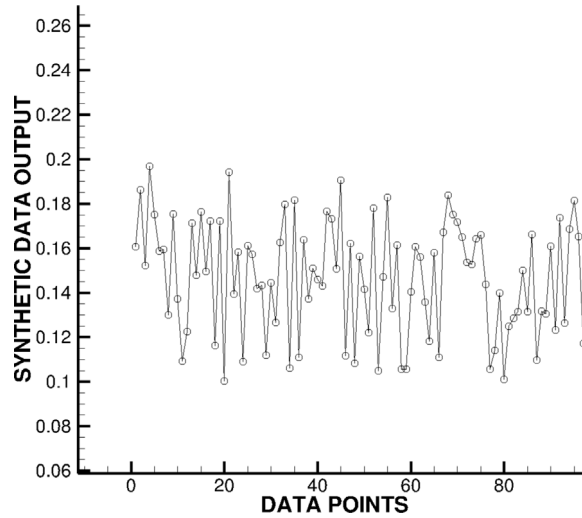


Fig. 8. One hundred synthetic data points used to train the Neural Net ( $\mathcal{O}^{Desired}$ ).

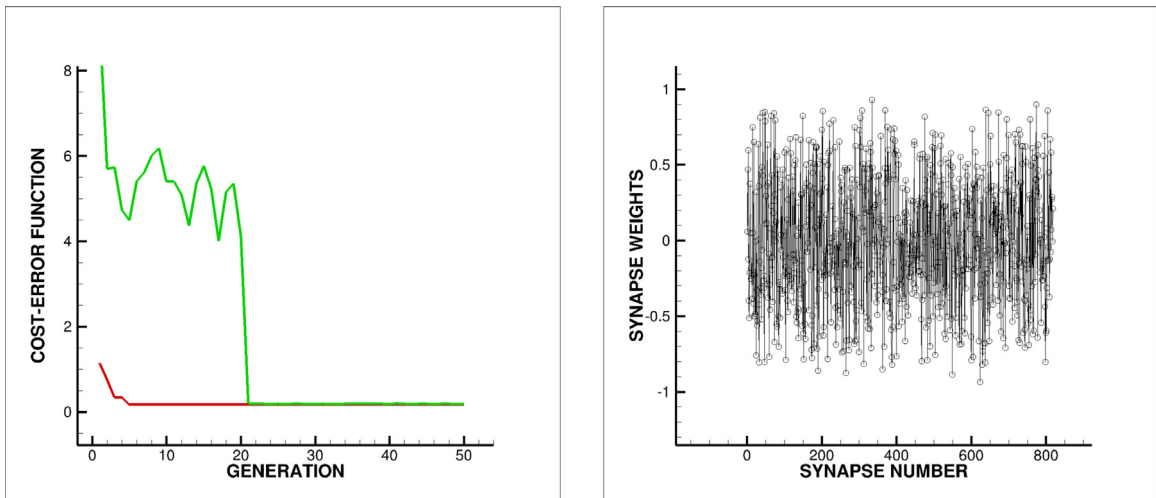
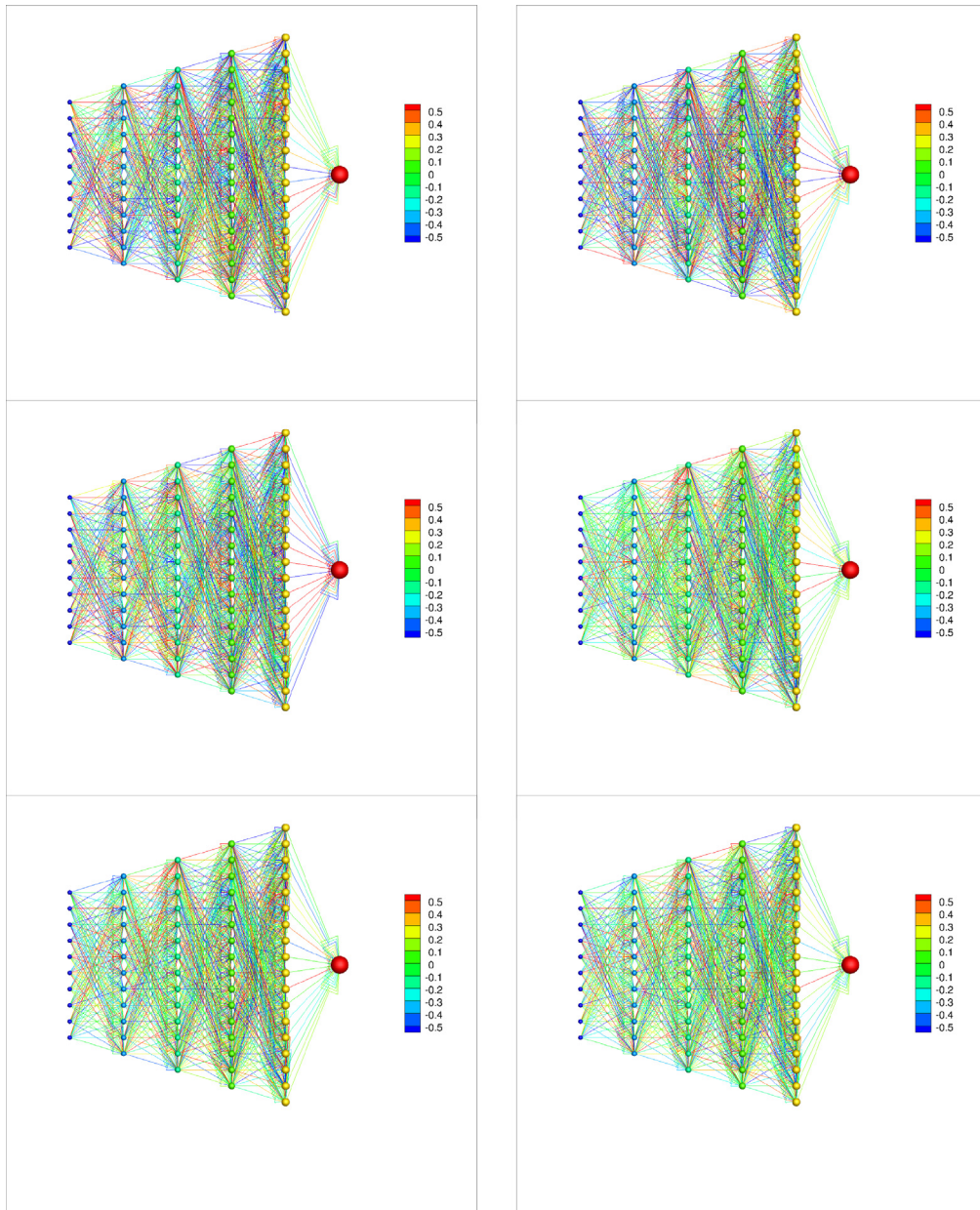


Fig. 9. Left: The reduction of error by the genetic-Machine Learning Algorithm (best performing gene (red) and the average of the population (green)). Right: The values optimized (818) synapse weights that comprise the design vector. The evolution of the best synapse weights, which stabilized after about 25 generations. From left to right and top to bottom at generations 1, 2, 4, 8, 16 and 32. The ANN is comprised of (1) Five layers (one input layer and four hidden layers) (2) 70 activation neurons (10 + 12 + 14 + 16 + 18) and (3)  $10 \times 12 + 12 \times 14 + 14 \times 16 + 16 \times 18 + 18 = 818$  weighted synapses. The color-coding represents the value of the synapse weights. (For interpretation of the references to color in this figure legend, the reader is referred to the web version of this article.)

cost function stabilized at  $\Pi \approx 0.176$  from a starting population average of  $\Pi \approx 8.305$ ; a reduction of error by a factor of  $\frac{\Pi^{start}}{\Pi^{end}} = 47.18$ . The refocussing was implemented at generation 20, which reduced the best gene’s cost function from approximately  $\Pi \approx 0.189$  to  $\Pi \approx 0.176$  over the course of generations 21 through 50. The approach is quite simple to implement and the entire 50 generation simulation, with 24 genes per evaluation (1200 total designs) took under a second on a laptop, making it ideal as a design tool. This example was representative of how this algorithm performed across a wide range of problems. Although the original computational model introduced earlier in the paper is extraordinarily fast, the ANN reduced order model accelerates simulations even further.



**Fig. 10.** The evolution of the best synapse weights, which stabilized after about 25 generations. From left to right and top to bottom at generations 1, 2, 4, 8, 16 and 32. The ANN is comprised of (1) Five layers (one input layer and four hidden layers) (2) 70 activation neurons (10 + 12 + 14 + 16 + 18) and (3)  $10 \times 12 + 12 \times 14 + 14 \times 16 + 16 \times 18 + 18 = 818$  weighted synapses. The color-coding represents the value of the synapse weights.

## 8. Summary

In summary, the objective of this work was to develop a flexible and rapidly computable framework that researchers can easily alter and manipulate to design solar-thermal storage and distribution systems. Specifically, this work developed a digital-twin Model to track and optimize the flow of solar power through a complex multistage solar-thermal storage system with customers drawing energy at peak hours. The method allows for a solar installation

performance to be tested quickly (in microseconds) for extremely long simulation periods, such as weeks, months and years using a genetic-based machine-learning digital-twin framework which integrates submodels for:

- optics and tracking of the Fresnel multi-mirror system,
- thermal absorption of the optical energy by the receiver and
- optimal operating temperature balancing radiative losses with heat storage.

The overall machine-learning digital-twin optimizes the configuration layout to balance meeting customer demands and operational efficiency. Numerical examples were provided to illustrate the approach. In addition to the motivation provided by the massive growth of data-centers and the corresponding need for precise energy management, another application of high interest is the development of combined solar-thermal and photovoltaic digital-twin technologies for sustainable continuous large-scale precision farming. There are two areas at the forefront which can immediately benefit from integration of a precisely controlled solar-thermal system:

- **LED-based indoor hydroponic farming:** Indoor farming “pods” consist of enclosed trailers with hydroponically grown plants, with energy supplied by carefully controlled LEDs, whereby a continuous and constant supply of nutrient-rich water that helps plants grow more consistently, using 90% less water than traditional agriculture with a customizable nutrient solution, using much fewer chemicals such as herbicides and pesticides, and avoiding an array of pathogens, such as salmonella and *E. coli*, which pose risks to human health. LED light strip “walls” provide crops with light from only the part of the spectrum they specifically need for photosynthesis, reducing energy waste in addition to capturing secondary reflections to maximize absorption efficiency. This technology supports the growth of the hydroponics industry, which is accelerating rapidly due to climate change, in addition to a more general trend of society transcending the archaic approach of outdoor farming of the last 10,000 years, which requires combatting insects, fungi and other plant pathogens.
- **Agrophotovoltaic systems:** Agrophotovoltaic (APV) systems attempt to co-develop the same area of land for both solar photovoltaic power and agriculture. APV systems were pioneered in the 1980s (Goetzberger and Zastrow [54]) and have steadily grown as photovoltaic systems have become more robust and inexpensive. We refer the reader to [28,54–77] for a broad survey of such systems.<sup>6</sup> However, as with all photovoltaic systems, they suffer from operation at night or peak hours, in particular if the system is greenhouse-based with 24 h growing cycles. Such systems can benefit greatly from integration with solar-thermal storage systems.

The integration of such agricultural systems with solar-thermal technologies and, more generally, Green Energy Management Systems, is underway by the author.

### Declaration of competing interest

The author declares that they have no known competing financial interests or personal relationships that could have appeared to influence the work reported in this paper.

### Data availability

No data was used for the research described in the article.

### Acknowledgments

This work has been partially supported by the UC Berkeley College of Engineering, USA and the USDA AI Institute for Next Generation Food Systems (AIFS), USA, USDA award number 2020-67021- 32855.

### References

- [1] T.I. Zohdi, An adaptive digital framework for energy management of complex multi-device systems, *Comput. Mech.* (2022) <http://dx.doi.org/10.1007/s00466-022-02212-8>.
- [2] Eric Masanet, Arman Shehabi, Nuo Lei, Sarah Smith, Jonathan Koomey, Recalibrating global data-center energy-use estimates, *Science* 367 (6481) (2020) 984–986.

<sup>6</sup> APV systems can involve a variety of aspects, even utilizing pollinating insects, such as bees, to “solar grazing” systems.

- [3] L. Belkhir, A. Elmeligi, Assessing ICT global emissions footprint: Trends to 2040 & recommendations, *J. Clean. Prod.* 177 (2018) 448–463.
- [4] N. Jones, How to stop data centres from gobbling up the worlds electricity, *Nature* 561 (7722) (2018) 163–166, <http://dx.doi.org/10.1038/D41586-018-06610-Y>, 2018.
- [5] Arman Shehabi, et al., United States Data-Center Energy Usage Report. No. LBNL-1005775, Lawrence Berkeley National Lab.(LBNL, Berkeley, CA (United States, 2016.
- [6] U.S. Department Of Energy, Annual energy outlook 2020, 2020, <https://www.eia.gov/Outlooks/Aeo/>.
- [7] U.S. Energy Information Administration, How much carbon dioxide is produced per kilowatthour of U.S. electricity generation, 2020.
- [8] R. Brown, E. Masanet, B. Nordman, W. Tschudi, A. Shehabi, J. Stanley, J. Koomey, D. Sartor, P. Chan, J. Loper, S. Capana, B. Hedman, R. Duff, E. Haines, D. Sass, A. Fanara, Report to Congress on Server and Data-Center Energy Efficiency: Public Law 109-431, Lawrence Berkeley National Laboratory, Berkeley, California, 2007, LBNL-363E..
- [9] E. Masanet, R.E. Brown, A. Shehabi, J.G. Koomey, B. Nordman, Estimating the energy use and efficiency potential of U.S. data-centers, *Proc. IEEE* 99 (8) (2011).
- [10] J.G. Koomey, Growth in Data-Center Electricity Use 2005 to 2010, Analytics Press, Oakland, California, 2011, <http://www.analyticspress.com/datacenters.html>.
- [11] F. Upton, North American energy security and infrastructure act of 2015. H.R. 8, in: 114th Congress, 2015, <https://www.congress.gov/bill/114th-congress/house-bill/8>.
- [12] Jonathan Koomey, Worldwide electricity used in data-centers, *Environ. Res. Lett.* 3 (034008) (2008) <http://stacks.iop.org/1748-9326/3/034008>.
- [13] Jonathan G. Koomey, Estimating total power consumption by servers in the U.S. and the world, 2007, <http://www.mediafire.com/file/exywo1hf6ionskw/AMDserverpowerusecomplete-final.pdf>.
- [14] W. Van Heddeghem, S. Lambert, B. Lannoo, D. Colle, M. Pickavet, P. Demeester, Trends in worldwide ICT electricity consumption from 2007 to 2012, *Comput. Commun.* 50 (2014) 64–76.
- [15] S. Lanzisera, B. Nordman, R.E. Brown, Data network equipment energy use and savings potential in buildings, *Energy Efficiency* 5 (2) (2012) 149–162.
- [16] P. Reviriego, J.A. Maestro, D. Larrabeiti, Burst transmission for energy-efficient ethernet, *IEEE Internet Comput.* 14 (4) (2010) 50–57.
- [17] D. Dudkowski, P. Hasselmeyer, Energy-efficient networking in modern data-centers, in: Konstantinos Samdanis, Peter Rost, Andreas Maeder, Michaela Meo, Christos Verikoukis (Eds.), *Green Communications: Principles, Concepts and Practice*, John Wiley & Sons, ISBN: 978-1-118-75926-4, 2015.
- [18] William Tschudi, Tengfang Xu, Dale Sartor, Jay Stein, High Performance Data Centers: A Research Roadmap, Lawrence Berkeley National Laboratory, Berkeley, CA, 2003, LBNL53483. [http://hightech.lbl.gov/documents/DataCenters\\_Roadmap\\_Final.pdf](http://hightech.lbl.gov/documents/DataCenters_Roadmap_Final.pdf).
- [19] Steve Greenberg, Evan Mills, Bill Tschudi, Peter Rumsey, Bruce Myatt, Best practices for data-centers: Lessons learned from benchmarking 22 data-centers, in: Proceedings of the ACEEE Summer Study on Energy Efficiency in Buildings in Asilomar, Vol. 3, ACEEE, CA, 2006, pp. 76–87, <http://eetd.lbl.gov/emills/PUBS/PDF/ACEEE-datacenters.pdf>.
- [20] C. Malone, C. Belady, Metrics to characterize datacenter & IT equipment energy use, in: Proceedings of the Digital Power Forum, Richardson, TX, 2006.
- [21] A. Sullivan, Energy star for data-centers, *Green Grid Forum* (2010) (2010).
- [22] I.H. Cheung, S. Greenberg, R. Mahdavi, R. Brown, W. Tschudi, Energy efficiency in small server rooms: Field surveys and findings, in: Proceedings the 2014 ACEEE Summer Study on Energy Efficiency in Buildings, 2014, LBNL- 6952E.
- [23] E. Masanet, A. Shehabi, L. Ramakrishnan, J. Liang, X. Ma, B. Walker, P. Mantha, California Berkeley, The Energy Efficiency Potential of Cloud-Based Software: A US Case Study, Lawrence Berkeley National Laboratory, 2013.
- [24] A. Shehabi, E. Masanet, H. Price, K. Traber, A. Horvath, W.W. Nazaroff, Data center design and location: Consequences for electricity use and greenhouse-gas emissions, *Build. Environ.* 46 (5) (2011).
- [25] J.G. Koomey, S. Berard, M. Sanchez, H. Wong, Implications of historical trends in the electrical efficiency of computing, *Ann. Hist. Comput.*, *IEEE* 33 (3) (2011) 46–54.
- [26] N. Horner, I. Azevedo, Power usage effectiveness in data-centers: overloaded and underachieving, *Electr. J.* 29 (4) (2016) 61–69, 2016.
- [27] A. Shehabi, S.J. Smith, N. Horner, I. Azevedo, R. Brown, J. Koomey, E. Masanet, D. Sartor, M. Herrlin, W. Lintner, United States Data-Center Energy Usage Report, Lawrence Berkeley National Laboratory, Berkeley, California, 2016, LBNL-1005775.
- [28] US National Renewable Energy Laboratory Website (NREL): <https://www.energy.gov/science-innovation/energy-sources/renewable-energy/solar>.
- [29] T.I. Zohdi, A digital-twin and machine-learning framework for precise heat and energy management of data-centers, *Comput. Mech.* (2022) 2022, <http://dx.doi.org/10.1007/s00466-022-02152-3>.
- [30] T.I. Zohdi, Computation of the coupled thermo-optical scattering properties of random particulate systems, *Comput. Methods Appl. Mech. Engrg.* 195 (2006a) 5813–5830.
- [31] T.I. Zohdi, On the optical thickness of disordered particulate media, *Mech. Mater.* 38 (2006b) 969–981.
- [32] T.I. Zohdi, F.A. Kuypers, Modeling and rapid simulation of multiple red blood cell light scattering, *Proc. R. Soc. Interface* 3 (11) (2006c) 823–831.
- [33] T.I. Zohdi, *Electromagnetic Properties of Multiphase Dielectrics. A Primer on Modeling, Theory and Computation*, Springer-Verlag, 2012.
- [34] T.I. Zohdi, A computational modeling framework for high-frequency particulate obscurant cloud performance, *Int. J. Eng. Sci.* 89 (2015) 75–85.
- [35] T.I. Zohdi, On high-frequency radiation scattering sensitivity to surface roughness in particulate media, *Comput. Part. Mech.* (2016) <http://dx.doi.org/10.1007/s40571-016-0118-3>.

- [36] T.I. Zohdi, Rapid simulation-based uncertainty quantification of flash-type time-of-flight and lidar-based body-scanning processes, *Comput. Methods Appl. Mech. Engrg.* (2019) <http://dx.doi.org/10.1016/j.cma.2019.03.056>.
- [37] H. Gross, in: H. Gross (Ed.), *Handbook of Optical Systems. Fundamental of Technical Optics*, Wiley-VCH, 2005.
- [38] J.D. Jackson, *Classical electrodynamics*, 1998.
- [39] T.I. Zohdi, Dynamic thermomechanical modeling and simulation of the design of rapid free-form 3D printing processes with evolutionary machine learning, *Comput. Methods Appl. Mech. Engrg.* 331 (1) (2018) 343–362, 2018.
- [40] T.I. Zohdi, Electrodynamic machine-learning-enhanced fault-tolerance of robotic free-form printing of complex mixtures, *Comput. Mech.* 63 (2019) 913–929, 2019.
- [41] Zohdi. T.I., A machine-learning framework for rapid adaptive digital-twin based fire-propagation simulation in complex environments, *Comput. Methods Appl. Mech. Eng.* 363 (2020) 112907.
- [42] T.I. Zohdi, A digital twin framework for machine learning optimization of aerial fire fighting and pilot safety, *Comput. Methods Appl. Mech. Engrg.* 373 (1) (2021) 113446, 2021.
- [43] T.I. Zohdi, A digital-twin and machine-learning framework for ventilation system optimization for capturing infectious disease respiratory emissions, *Arch. Comput. Methods Eng.* (2021) <http://dx.doi.org/10.1007/s11831-021-09609-3>.
- [44] T.I. Zohdi, A digital-twin and machine-learning framework for the design of multiobjective agrophotovoltaic solar farms, *Comput. Mech.* (2021) <http://dx.doi.org/10.1007/s00466-021-02035-z>.
- [45] J.H. Holland, *Adaptation in Natural & Artificial Systems*, University of Michigan Press, Ann Arbor, Mich, 1975.
- [46] J.H. Holland, J.H. Miller, Artificial adaptive agents in economic theory (PDF), *Amer. Econ. Rev.* 81 (2) (1991) 365–371, Archived from the original (PDF) on October 27, 2005.
- [47] D.E. Goldberg, *Genetic Algorithms in Search, Optimization & Machine Learning*, Addison-Wesley, 1989.
- [48] L. Davis, *Handbook of Genetic Algorithms*, Thompson Computer Press, 1991.
- [49] C. Onwubiko, *Introduction to Engineering Design Optimization*, Prentice Hall, 2000.
- [50] D.E. Goldberg, K. Deb, Special issue on genetic algorithms, *Comput. Methods Appl. Mech. Eng.* 186 (2–4) (2000) 121–124.
- [51] D. Luenberger, *Introduction to Linear & Nonlinear Programming*, Addison-Wesley, Menlo Park, 1974.
- [52] P. Gill, W. Murray, M. Wright, *Practical Optimization*, Academic Press, 1995.
- [53] T.I. Zohdi, 193. Zohdi, T.I. (2022) A note on rapid genetic calibration of artificial neural networks, *Comput. Mech.* (2022) <http://dx.doi.org/10.1007/s00466-022-02216-4>.
- [54] A. Goetzberger, A. Zastrow, On the coexistence of solar-energy conversion and plant cultivation, *Int. J. Sol. Energy* (ISSN: 0142-5919) 1 (1) (1982) 55–69, <http://dx.doi.org/10.1080/01425918208909875>.
- [55] Harshavardhan Dinesh, Joshua M. Pearce, The potential of agrivoltaic systems, *Renew. Sustain. Energy Rev.* 54 (2016) 299–308, <http://dx.doi.org/10.1016/j.rser.2015.10.024>.
- [56] C. Dupraz, H. Marrou, G. Talbot, L. Dufour, A. Nogier, Y. Ferard, Combining solar photovoltaic panels and food crops for optimizing land use: towards new agrivoltaic schemes, *Renew. Energy* 36 (2011a) 2725–2732, <http://dx.doi.org/10.1016/j.renene.2011.03.005>.
- [57] W. Liu, L. Liu, G. Guan, F. Zhang, M. Li, P. Lv, J. Ingenhoff, A novel agricultural photovoltaic system based on solar spectrum separation, *Sol. Energy* 162 (1) (2018) 84–94, 2018.
- [58] P.R. Malu, U.S. Sharma, J.M. Pearce, Agrivoltaic potential on grape farms in India, *Sustain. Energy Technol. Assess.* 23 (2017) 104–110, <http://dx.doi.org/10.1016/j.seta.2017.08.004>.
- [59] S. Castellano, Photovoltaic greenhouses: evaluation of shading effect and its influence on agricultural performances, *J. Agric. Eng.* (ISSN: 2239-6268) 45 (4) (2014) 168–175, <http://dx.doi.org/10.4081/jae.2014.433>.
- [60] A. Weselek, A. Ehmann, S. Zikeli, I. Lewandowski, S. Schindele, P. Hogy, Agrivoltaic systems: applications, challenges, and opportunities. A review, *Agron. Sustain. Dev.* 39 (2019) Article number: 35.
- [61] S. Amaducci, X. Yin, M. Colauzzi, Agrivoltaic systems to optimise land use for electric energy production, *Appl. Energy* 220 (2018) 545–561, <http://dx.doi.org/10.1016/j.apenergy.2018.03.081>.
- [62] A. Armstrong, N.J. Ostle, J. Whitaker, Solar park microclimate and vegetation management effects on grassland carbon cycling, *Environ. Res. Lett.* 11 (74016) (2016) <http://dx.doi.org/10.1088/1748-9326/11/7/074016>.
- [63] G.A. Barron-Gafford, R.L. Minor, N.A. Allen, A.D. Cronin, A.E. Brooks, M.A. Pavao-Zuckerman, The photovoltaic heat island effect: larger solar power plants increase local temperatures, *Sci. Rep.* 6 (35070) (2016) <http://dx.doi.org/10.1038/srep35070>.
- [64] M. Cossu, L. Murgia, L. Ledda, P.A. Deligios, A. Sirigu, F. Chessa, A. Pazzona, Solar radiation distribution inside a greenhouse with south-oriented photovoltaic roofs and effects on crop productivity, *Appl. Energy* 133 (2014) 89–100, <http://dx.doi.org/10.1016/j.apenergy.2014.07.070>.
- [65] M. Cossu, A. Yano, Z. Li, M. Onoe, H. Nakamura, T. Matsumoto, J. Nakata, Advances on the semi-transparent modules based on micro solar cells: first integration in a greenhouse system, *Appl. Energy* 162 (2016) 1042–1051, <http://dx.doi.org/10.1016/j.apenergy.2015.11.002>.
- [66] Y. Elamri, B. Cheviron, J.-M. Lopez, C. Dejean, G. Belaud, Water budget and crop modelling for agrivoltaic systems: application to irrigated lettuces, *Agric. Water Manag.* 208 (2018) 440–453, <http://dx.doi.org/10.1016/j.agwat.2018.07.001>.
- [67] Y. Elamri, B. Cheviron, A. Mange, C. Dejean, F. Liron, G. Belaud, Rain concentration and sheltering effect of solar panels on cultivated plots, *Hydrol. Earth Syst. Sci. Discuss.* (2017) 1–37, <http://dx.doi.org/10.5194/hess-2017-418>.
- [68] Shiva Gorjian, Francesco Calise, Karunesh Kant, Md Shamim Ahamed, Benedetta Copertaro, Gholamhassan Najafi, Xingxing Zhang, Mohammadreza Aghaei, Redmond R. Shamschiri, A review on opportunities for implementation of solar energy technologies in agricultural greenhouses, *J. Clean. Prod.* (ISSN: 0959-6526) 285 (2021) 124807, <http://dx.doi.org/10.1016/j.jclepro.2020.124807>.
- [69] M. Homma, T. Doi, Y. Yoshida, A field experiment and the simulation on agrivoltaic-systems regarding to rice in a paddy field, *J. Jpn. Soc. Energy Resour.* 37 (2016) 23–31, [http://dx.doi.org/10.24778/jjser.37.6\\_23](http://dx.doi.org/10.24778/jjser.37.6_23).

- [70] D. Majumdar, M.J. Pasqualetti, Dual use of agricultural land: introducing agrivoltaics in phoenix metropolitan statistical area, USA *Landsc. Urban Plan.* 170 (2018) 150–168, <http://dx.doi.org/10.1016/j.landurbplan.2017.10.011>.
- [71] H. Marrou, L. Dufour, J. Wery, How does a shelter of solar panels influence water flows in a soil-crop system? *Eur. J. Agron.* 50 (2013a) 38–51, <http://dx.doi.org/10.1016/j.eja.2013.05.004>.
- [72] H. Marrou, L. Guillioni, L. Dufour, C. Dupraz, J. Wery, Microclimate under agrivoltaic systems: is crop growth rate affected in the partial shade of solar panels? *Agric. Meteorol.* 177 (2013b) 117–132, <http://dx.doi.org/10.1016/j.agrformet.2013.04.012>.
- [73] H. Marrou, J. Wery, L. Dufour, C. Dupraz, Productivity and radiation use efficiency of lettuces grown in the partial shade of photovoltaic panels, *Eur. J. Agron.* 44 (2013c) 54–66, <http://dx.doi.org/10.1016/j.eja.2012.08.003>.
- [74] P. Santra, P. Pande, S. Kumar, D. Mishra, R. Singh, Agri-voltaics or solar farming: the concept of integrating solar PV based electricity generation and crop production in a single land use system, *Int. J. Renew. Energy Res.* 7 (2017).
- [75] Max Trommsdorff, Jinsuk Kang, Christian Reise, Stephan Schindele, Georg Bopp, Andrea Ehmann, Axel Weselek, Petra Hogy, Tabea Obergfell, Combining food and energy production: Design of an agrivoltaic system applied in arable and vegetable farming in Germany, *Renew. Sustain. Energy Rev.* 140 (2021) 110694, <https://www.sciencedirect.com/science/article/pii/S1364032120309783>.
- [76] A. Weselek, A. Ehmann, S. Zikeli, et al., Agrophotovoltaic systems: applications, challenges, and opportunities. a review, *Agron. Sustain. Dev.* 39 (2019) 35, <http://dx.doi.org/10.1007/s13593-019-0581-3>.
- [77] B. Valle, T. Simonneau, F. Sourd, P. Pechier, P. Hamard, T. Frisson, M. Ryckewaert, A. Christophe, Increasing the total productivity of a land by combining mobile photovoltaic panels and food crops, *Appl. Energy* 206 (2017) 1495–1507, <http://dx.doi.org/10.1016/j.apenergy.2017.09.113>.